Journal of plankton research
April 2024, Volume 46, Issue 2, Pages 100-116
https://doi.org/10.1093/plankt/fbad061 https://archimer.ifremer.fr/doc/00876/98830/

Photoacclimation in the kleptoplastidic ciliate *Mesodinium rubrum* and its cryptophyte prey *Teleaulax amphioxeia*: phenotypic variability and implications for red tide remote sensing

Pochic Victor [1, 2, *], Gernez Pierre [1], Zoffoli Maria Laura [3], Sechet Veronique [2], Carpentier Liliane [2], Lacour Thomas [2]

[1] Nantes Université, Institut des Substances et Organismes de la Mer , ISOMER, UR 2160, F-44000 Nantes , France
[2] Ifremer, PHYTOX, Laboratoire PHYSALG , F-44000 Nantes , France
[3] Consiglio Nazionale delle Ricerche, Istituto di Scienze Marine (CNR-ISMAR) , 00133 Rome , Italy

* Corresponding author : Victor Pochic, email address : victor.pochic@univ-nantes.fr

Abstract :

Mesodinium rubrum is a kleptoplastidic ciliate that sequesters the chloroplasts and nuclei of cryptophyte algae to perform photosynthesis. Blooms of M. rubrum can cause red tides in coastal oceans worldwide. Such red tides are detectable by remote sensing, and studying M. rubrum pigments and optical properties is a crucial step toward characterizing its blooms using satellite observation. Previous studies have shown that M. rubrum photoacclimates, modifying its pigment content depending on irradiance. Using cultures at different irradiance levels, we observed that photoacclimation in M. rubrum closely resembles that of its cryptophyte prey Teleaulax amphioxeia, leading to substantial phenotypic variability. In both species, phycoerythrin 545 cellular concentrations increased 3-fold between the highest and lowest irradiance, suggesting a major role in photoacclimation. Absorption cross-section decreased, and pigment-specific absorption coefficients increased with irradiance at the peak absorption wavelengths of chlorophyll a and phycoerythrin 545. After assessing the variability of absorption properties in M. rubrum, we combined field measurements and high-resolution Sentinel-2 satellite images to estimate chlorophyll a concentration of a coastal red tide and document small-scale spatio-temporal features. This work provides an overview of pigment photoacclimation in a peculiar phytoplankter and suggests guidelines for future studies of M. rubrum blooms.

Keywords : Mesodinium, photoacclimation, phycoerythrin, bloom, remotesensing

Introduction

Mesodinium rubrum (Lohmann, 1908) is a cosmopolitan planktonic ciliate, occurring in marine environments ranging from polar to subtropical latitudes (Moeller *et al.*, 2011; Guzmán *et al.*, 2016). High-biomass blooms of this ciliate can lead to spectacular dark red seawater discolorations, and *M. rubrum* red tides have been observed in a variety of coastal systems worldwide (Crawford, 1989). These phenomena have been documented at least since Darwin's voyage on the *Beagle*, during which he gave a striking description of a *M. rubrum* red tide and of the then unnamed animalcule that was causing it (Darwin, 1839; Hart, 1943). *M. rubrum*'s ability to form massive blooms can be surprising because this unicellular organism relies on predation for photosynthetic growth. *M. rubrum* is an obligate mixotroph that preys on cryptophyte algae and keeps their chloroplasts and nuclei inside its own cytoplasm to perform photosynthesis (Gustafson *et al.*, 2000). *M. rubrum* is capable of replicating the stolen chloroplasts during cell division, but not the stolen nucleus (kleptokaryon), and therefore needs to prey regularly on cryptophytes to keep its photosynthetic abilities and survive (Kim *et al.*, 2017). *M. rubrum* is also known for being the prey of the kleptoplastidic dinoflagellate *Dinophysis*, a producer of toxins that can cause diarrhetic shellfish poisoning (DSP) (Park *et al.*, 2006; Minnhagen *et al.*, 2011). *Dinophysis* harmful algal blooms (HABs) constitute a major threat for public health and shellfish farming in coastal areas worldwide (Díaz *et al.*, 2019; Mafra *et al.*, 2019; Guillotreau *et al.*, 2021). Studying the ecophysiology and bloom phenology of the species involved in the *Dinophysis* trophic chain is therefore crucial to better understand DSP outbreaks, anticipate, and manage the risk of DSP events.

A specific trait shared by all three organisms of the *Dinophysis* trophic chain is the presence of phycobiliproteins (PBP) in their plastids. Phycobiliproteins are hydrosoluble photosynthetic pigments, only present in the plastids of cryptophytes, cyanobacteria and red algae, which play a key role in the photoacclimation of these organisms to low light environments (Zhao *et al.*, 2011; Richardson, 2022). All phycobiliproteins share the same basic molecular structure: one apoprotein linked to several chromophores, the phycobilins. Nonetheless, cryptophycean PBP differ from their cyanobacterial and red algal counterparts by their quaternary structure and their cellular localization (Overkamp *et al.*, 2014). More specifically, phycoerythrin 545 (PE 545) is a major photosynthetic pigment in the cryptophyte genus *Teleaulax*, one of *M. rubrum*'s main prey (**Fig. 1A-D**) (Peltomaa and Johnson, 2017; Altenburger *et al.*, 2021). PE 545 is rarely quantified in studies of *M. rubrum* pigment composition (Rial *et al.*, 2013; Gaillard *et al.*, 2020), although it significantly contributes to

light absorption in this organism via a broad absorption peak in the green region (475 – 600 nm), with a maximum at 545 nm (Barber *et al.*, 1969; Altenburger *et al.*, 2020; Gernez *et al.*, 2023). Identifying PE 545 dynamics in relation with growth conditions is therefore important for understanding the photophysiology of this ciliate.

In the dynamic ocean, planktonic organisms are exposed to multi-scale variations in light exposure caused by meteorological variability, vertical mixing, and variations in seawater bio-optical properties (Denman and Gargett, 1983; Lacour *et al.*, 2017). Phytoplankton are particularly effective in adjusting their metabolism to their environment which varies in irradiance intensity and spectral composition (Stramski *et al.*, 1993; Jaubert *et al.*, 2017). Photoacclimation, the ability of an algal cell to modify its metabolism - including its pigment phenotype - depending on irradiance (MacIntyre *et al.*, 2002), is a well-documented phenomenon in many taxa, including cryptophytes (Sciandra *et al.*, 2000; Laviale and Neveux, 2011; Heidenreich and Richardson, 2020). It has been established that *M. rubrum* inherits at least some photoacclimation abilities from its prey upon sequestration of their organelles. Moeller *et al.* (2011) have documented photoacclimation in a polar strain of *M. rubrum*, with cellular concentrations of chlorophyll *a* (chl *a*) and phycoerythrin decreasing as irradiance increases. Recent studies on photoacclimation in both *M. rubrum* and its prey *Teleaulax amphioxeia* showed that while the ciliate is able to photoacclimate, the precise mechanisms involved in the process are still unknown because *Mesodinium* does not display the light-dependent transcriptional changes of photosynthesis-related genes that occur in its prey (Altenburger *et al.*, 2021; Johnson *et al.*, 2023). In this regard, the extent to which photoacclimation in *M. rubrum* is similar to its prey remains an open question, particularly regarding its ability to adjust PE 545 concentration.

Beside its importance in eco-physiological studies, developing a better understanding of *M. rubrum* photoacclimation is of interest for optical modelling and remote sensing applications. During bloom events, dark red patches stretching over several kilometers can be detected from high-resolution satellite images due to the influence of *M. rubrum*'s PE 545 on seawater optical properties (Dierssen *et al.*, 2015; Gernez *et al.*, 2023). However, a detailed characterization of *M. rubrum*'s inherent optical properties (IOPs) is needed to develop an optical model able to unambiguously identify a bloom dominated by *M. rubrum*, and accurately assess its biomass from satellite observation (Guzmán *et al.*, 2016). In particular, the thorough determination of *M. rubrum*'s chl *a* specific absorption coefficient, as well as its range of variability, is a prerequisite to the development of a bio-optical model that could quantitatively be used in red tide remote sensing (Craig *et al.*, 2006; Leong and Taguchi, 2006).

In the present article, we present the results of two photoacclimation experiments. In the first one, we measured the photoacclimation response of *M. rubrum* cultures exposed to 4 levels of irradiance, after a 5-day acclimation period. In the second experiment, we compared the photoacclimation response of both *M. rubrum* and *T. amphioxeia,* acclimated to 3 levels of irradiance over a period of 12 days. From these experiments, we measured the growth rate, absorption coefficient, and pigment content of both species, including the hydrosoluble phycoerythrin 545. We then compared the absorption coefficients and pigment compositions measured on cultures to field and laboratory data from the literature, and to that of field samples acquired during a red tide of *M. rubrum*. Finally, we assessed the influence of the range of variability in *M. rubrum*'s chl *a*-specific absorption coefficient on chl *a* estimation using a standard remote-sensing algorithm (Gons *et al.*, 2002), and computed maps of chl *a* concentration during a bloom of *M. rubrum* observed at high spatial resolution with the Sentinel-2 satellite mission. These maps allowed us to document small-scale features of the bloom surface distribution, as well as its rapid temporal evolution.

Methods

Photoacclimation experiments

T. amphioxeia (strain AND-A0710, 2007, Huelva, Southwestern Spain) and *M. rubrum* (strain MrDK-2009, 2009, Helsingør harbor, Denmark) cultures were grown in 35 mL of pre-filtered L1 medium (Guillard and Hargraves, 1993), in 50 mL glass Erlenmeyer flasks. Two independent experiments were conducted. In the first one, *M. rubrum* cultures were maintained at 17.5°C, under 12/12h light/dark illumination, provided by white fluorescent tubes (**Fig. S1**) at 20, 65, 120 and 220 µmol photons.m^{-2}.s^{-1}, as measured with a LI-250A Light Meter (LI-COR Biosciences) in air mode. The kleptoplastidic ciliate *M. rubrum* was fed with *T. amphioxeia* (grown at 17.5°C and 65 µmol photons.m^{-2}.s^{-1}) on day 0, at a prey-predator ratio of 3:1. This first photoacclimation experiment lasted for 5 days, at the end of which cultures were sampled for analysis. In the second experiment, semicontinuous cultures of *T. amphioxeia* and *M. rubrum* were grown at 21°C, in a 12/12h light/dark cycle at irradiances of 20, 80 and 200 µmol photons.m^{-2}.s^{-1}. The acclimation period lasted for 12 days, during which *M. rubrum* was fed with *T. amphioxeia* (grown at 20 µmol photons.m^{-2}.s^{-1}) every 3 days at a ratio of 3 prey cells for 1 predator. Cultures were sampled for analysis at the end of the acclimation period.

During the first experiment, cell counts and equivalent spherical diameter (ESD) of the microalgal cells were monitored at the start (day 0) and at the end (day 5) of the experiment, with a particle

counter (Multisizer 3, Beckmann-Coulter). During the second experiment, cell counts, chl *a* fluorescence and PE 545 fluorescence were monitored daily with a flow cytometer (MACSQuant 10, Miltenyi Biotec), while ESD of the cells were measured with the particle counter on the final day of the experiment. Daily monitoring confirmed that cryptophytes were promptly consumed by the ciliates, within a day after the feeding. In cultures of *M. rubrum* at 80 and 200 µmol photons.m^{-2}.s^{-1} at 21°C, a contamination of the cultures by small-sized brown microalgae was identified by an unexpected population of relatively small, chl *a*-containing cells in the cytograms and confirmed by the detection of the carotenoids fucoxanthin and diadinoxanthin/diatoxanthin in these cultures (**Fig. S2**). Nonetheless, the low concentration of contaminating cells (< 7% of total cell biovolume) is unlikely to have significantly influenced the physiological response of *M. rubrum*. Predation of *M. rubrum* on these contaminating brown algae is unlikely due to its strict prey selectivity towards certain cryptophytes (Peltomaa and Johnson, 2017). However, we cannot rule out the fact that some slight allelopathic effects from the brown algae towards the ciliate influenced the latter's physiology. We need to consider however that because of this contamination, the concentrations of chl *a* and chl c_2 attributed to *M. rubrum* in these cultures were slightly overestimated. Occasional contaminations of *M. rubrum* cultures by the small chrysophyte *Ochromonas sp.* were reported by Hernández-Urcera *et al.* (2018). Although the contaminating algae in our study were not *Ochromonas* (no violaxanthin/zeaxanthin detected), it testifies to the difficulty of growing pure cultures of *M. rubrum* in undiluted culture medium.

The relationship between the growth rate (µ, d^{-1}) and growth irradiance (E, µmol photons.m^{-2}.s^{-1}) was modelled by fitting to the data the following equation, as suggested by MacIntyre *et al.* (2002):

$$\mu = \mu_m(1 - \exp\left(\frac{-E}{K_E}\right)) \qquad \textit{Equation 1.}$$

where μ_m is the maximum growth rate (in d^{-1}) and K_E is the light saturation parameter for growth (in µmol photons.m^{-2}.s^{-1}). The relationship was fitted to the data by non-linear least-squares.

For the measurement of lipophilic pigments and absorption coefficients, samples were filtered onto 0.2 µm-pore glass fiber filters (Whatman, grade GF/F) and stored at -80°C. For PBP measurements, samples of cultures were centrifuged at 4100g for 10 minutes. A cell count was performed on the supernatant after the centrifugation, to assess the proportion of cells that were missing in the pellet. The pellets were then stored at -80°C. For the second experiment only, 5 mL of each culture were sampled for in vivo absorption measurements that were done within 4 hours after sampling.

Extraction and quantification of lipophilic pigments

Filters sampled for pigment analysis were immersed into 2 mL of 95% acetone, sonicated for 10 minutes in an ultrasonic water bath (Advantage Lab) and thawed at -20°C for 24h. Extracts were then filtered onto a 0.2 µm-pore PTFE membrane filter (Whatman), before injection in high performance liquid chromatography (HPLC). The concentrations of lipophilic pigments in the extracts were measured by HPLC-UV-DAD (series 1200; Agilent Technologies) using an Eclipse XDB-C8 reverse phase column (150 mm × 4,6 mm, 3.5 µm particle size; Agilent Technologies). For one condition (*M. rubrum*, 17.5°C, 65 µmol photons.m^{-2}.s^{-1}), the sample of one replicate was degraded and the resulting pigment concentrations were uninterpretable.

Extraction and quantification of phycoerythrin 545

Phycobiliproteins were extracted following the protocol recommended by Lawrenz *et al.* (2011). The pellets were unfrozen and suspended in 4 mL of 0.1M Na-phosphate buffer (pH=6.3; Gomori, 1955), sonicated for 10 minutes, then left to thaw at 4°C for 24h. The extracts were then centrifuged (4100g, 10 minutes). For each sample, a volume of 200 µL of supernatant, containing the extracted PE 545, was filtered on a 0.2 µm-pore polyethersulfone (PES) filter to eliminate minute cell parts containing lipophilic pigments. The optical density (OD) of the filtered supernatant was then measured from 400 – 750 nm with a 96-well plate-reading spectrophotometer (Tecan, Infinite200Pro). The solution of phosphate buffer used for the extraction was taken as reference. The value of OD at 750 nm was subtracted throughout the spectrum as correction, because the absorption of PE 545 is null in the near-infrared spectral range. The concentration of PE 545 ([PE 545], in mg.L^{-1}) was calculated from the OD at the peak of absorption at 552 nm using an equation adapted from Cunningham *et al.*, (2019):

$$[\text{PE 545}] = \frac{\text{OD}_{\text{max}}+(\text{OD}_{\text{max}}\times \text{p}_{\text{surn}})}{\varepsilon \times d} \times \frac{V_{\text{b}}}{V_{\text{s}}} \times 10^{3} \qquad \textit{Equation 2.}$$

With OD_{max} the OD at the absorption peak, p_{surn} the percentage of cells remaining in the supernatant after culture centrifugation (7% for *T. amphioxeia*, 0% for *M. rubrum*); ε the mass extinction coefficient of PE 545: ε = 12.6 L.g^{-1}.cm^{-1} (MacColl *et al.*, 1976); d the optical path length through the solution (0.579 cm); V_{b} the volume of phosphate buffer (4 mL); V_{s} the volume of culture sampled (10 mL). A molar mass $\text{MW}_{\text{PE 545}}$ = 57.03 kDa was used to convert the mass of PE 545 into moles (Protein Data Bank, code 1XF6, data from Doust *et al.*, 2004).

Measurement of microalgae absorption

The coefficient of particulate absorption, $a_{\text{p}}(\lambda)$, was measured *in vivo* from 350 – 850 nm using a dual beam spectrophotometer equipped with a 150 mm integrating sphere (Perkin-Elmer, Lambda 1050). Compared to other techniques (i.e. filter pad), measuring $a_{\text{p}}(\lambda)$ on a suspension of living cells

placed inside an integrating sphere was demonstrated as being the most accurate method (Röttgers and Gehnke, 2012; Stramski et al., 2015). A 1 cm-width quartz cuvette containing a small volume of the culture was placed in the middle of the sphere using a white holder provided by the manufacturer. The coefficient of total absorption, a (λ), was computed as:

$$a(\lambda) = \ln(10) \times \frac{\mathrm{OD_s}(\lambda)}{d} \qquad \textit{Equation 3.}$$

With OD_s the OD of the living cells suspended in the cuvette; d the optical path length in the cuvette (0.01 m). The absorption of the suspended particles was then computed by subtracting the contribution of pure seawater and of coloured dissolved organic matter (CDOM), which was measured on the filtrate of culture samples filtered on a 0.2 µm-pore PES filter:

$$a_p(\lambda) = a(\lambda) - a_w(\lambda) - a_{cdom}(\lambda) \qquad \textit{Equation 4.}$$

In the remaining of the present study, $a_p(\lambda)$ will refer to *in vivo* particulate absorption measurements, unless specified otherwise. In order to compare with the filter pad method, the coefficient of particulate absorption was also measured on GF/F filters using the same spectrophotometer. The optical density (OD) was measured on unfrozen GF/F filters, with the filter placed inside the integrating sphere. The coefficient of particulate absorption was computed in two steps. First, the absorption by particles was computed from OD without correction for pathlength amplification:

$$a_p^{\mathrm{uncorr}}(\lambda) = \frac{\ln(10) \times \mathrm{OD_f} \times A_f}{V} \qquad \textit{Equation 5.}$$

With OD_f the OD measured on the filter; A_f the area of the coloured zone on the filter; and V the filtered volume. Second, the pathlength amplification was corrected individually for each sample using the *in vivo* $a_p(\lambda)$ as the reference for true absorption, following an approach proposed by Röttgers and Gehnke (2012). Correcting for pathlength amplification is required when using the filter-pad technique because scattering in the particle/filter matrix lengthens the distance travelled by photons, thus significantly increasing OD measurements (Bricaud and Stramski, 1990). For comparison purposes, the coefficient of particulate absorption was also computed using a non-specific pathlength correction (Stramski *et al.*, 2015). Both methods for pathlength amplification correction are detailed in Suppl. Info. 1. The contribution of non-pigmented particles to $a_p(\lambda)$ was not measured in the cultures.

Calculation of absorption cross section and pigment-specific absorption

The absorption cross-section, σ_a, in $m^2.cell^{-1}$, indicates the absorptive power of one algal cell (Stramski and Mobley, 1997). It was computed as:

$$\sigma_a(\lambda) = \frac{a_p(\lambda)}{N} \qquad \textit{Equation 6.}$$

With N the cell density of the sample (in cells.m^{-3}); $a_p(\lambda)$ is the coefficient of particulate absorption.

The pigment-specific absorption coefficient, a_p^*, in m^2.mg$_{pigment}^{-1}$ indicates the efficiency of the absorption by pigments in the cells (Bricaud *et al.*, 1995). Here we focused on the pigment-specific absorption at 552 and 675 nm, which correspond to the maximum absorption wavelengths of PE 545 and chl *a*, respectively, and for which most of the absorption is due to that pigment:

$$a_p^*(675) = \frac{a_p(675)}{[\text{chl } a]} \qquad \textit{Equation 7a.}$$

$$a_p^*(552) = \frac{a_p(552)}{[\text{PE } 545]} \qquad \textit{Equation 7b.}$$

With $a_p(\lambda)$ the particulate absorption at wavelength λ (in m^{-1}); and [pigment] the concentration of the pigment responsible for absorption at the same wavelength (in mg.m^{-3}). Additionally, the specific absorption coefficient of chl *a* at 665 nm, $a_p^*(665)$ was calculated and used for the analysis of field and satellite radiometric measurements.

M. rubrum *bloom observations*

Field sampling

In situ samples were collected at 8 stations during a *M. rubrum* bloom off the French Atlantic coast on 29 March 2021 (**Fig. 1E-G**). Water samples were collected at the surface using a bucket, gently stirred to homogenise phytoplankton concentration, and poured into 2L bottles. Bottles were conserved in the dark at ambient temperature until subsequent laboratory analyses, within 2 – 4 hours after sampling. Back in the laboratory, the samples were filtered on GF/F filters and stored at -80°C until pigments analysis by HPLC. The particulate absorption coefficient was measured on filters as described earlier. Pathlength amplification was corrected with the two methods mentioned previously and detailed in Suppl. Info. 1. To better compare with microalgae culture, the particulate absorption coefficient measured on *in situ* samples was further partitioned into absorption by phytoplankton, $a_{phy}(\lambda)$, and by non-pigmented particles, using bleach for pigment extraction (Roesler *et al.*, 2018).

Above-water radiometric measurements were performed concomitantly to water sampling. The upwelling radiance, $L_u(\lambda)$, downwelling radiance, $L_d(\lambda)$, and sky radiance, $L_{sky}(\lambda)$, were sequentially measured following a standard protocol (Mueller et al., 2003) using a hand-held spectroradiometer (ASD Fieldspec, HandHeld 2). The air-water interface reflection coefficient of the sky radiance, ρ,

was calculated as a function of wind speed, sea state, sky conditions and geometry of acquisition at the time of field measurement (Ruddick *et al.*, 2006). The remote sensing reflectance, $R_{rs}(\lambda)$, was computed as:

$$R_{rs}(\lambda) = \frac{L_u(\lambda) - \rho\, L_{sky}(\lambda)}{\pi\, L_d(\lambda)} \qquad \textit{Equation 8.}$$

Satellite data acquisition and processing

On-board Sentinel-2 (S2), the multi-spectral imager (MSI) makes it possible to observe phytoplankton coastal blooms at high spatial resolution (Caballero *et al.*, 2020). Here, two S2 images were available during the *M. rubrum* red tide on the 27 and 29 March 2021 (**Fig. 1F-G**), and used to map chl *a* concentration ([chl *a*]). Top-of-atmosphere Level-1C products were downloaded from the Copernicus open access hub (https://dataspace.copernicus.eu/) and resampled at 20 m. The GRS algorithm for atmospheric correction and sunglint removal (Harmel *et al.*, 2018) was applied to L1C data to retrieve the bottom-of-atmosphere spectral remote-sensing reflectance, $R_{rs}(\lambda)$. The GRS atmospheric correction was previously validated during high biomass phytoplankton blooms, including red tides of *M. rubrum* (Gernez *et al.*, 2023).

For each pixel, chl *a* was computed from $R_{rs}(\lambda)$ using a semi-analytical red-edge algorithm (Gons, 1999; Gons *et al.*, 2002) recalibrated for S2/MSI (Gernez *et al.*, 2017). This algorithm is based on the common radiative transfer approximation (Morel and Prieur, 1977):

$$R_{rs}(\lambda) \sim \frac{b_b(\lambda)}{b_b(\lambda)+a(\lambda)} \qquad \textit{Equation 9.}$$

The backscattering coefficient, b_b, is computed from $R_{rs}(\lambda)$ at 783 nm using the assumption that in the near-infrared spectral range the absorption coefficient is dominated by pure seawater:

$$b_b = \frac{1.56\,\pi\, R_{rs}(783)}{0.082 - 0.6\,\pi\, R_{rs}(783)} \qquad \textit{Equation 10.}$$

Then, $a_{phy}(665)$ is retrieved from the red-edge band ratio $R_{rs}(705)/R_{rs}(665)$, assuming that b_b is spectrally neutral from 665 – 783 nm, and that at 665 and 705 nm the absorption coefficient by non-algal particles and CDOM is negligible compared to that of chl *a* and pure seawater:

$$a_{phy}(665) = (0.7 + b_b)\frac{R_{rs}(705)}{R_{rs}(665)} - 0.4 - {b_b}^{p} \qquad \textit{Equation 11.}$$

The tuning parameter, p, was set to 1.02 (Gernez *et al.*, 2017).

Finally, the chl *a* concentration is computed from $a_{phy}(665)$ using:

$$[\text{chl } a] = \frac{a_{\text{phy}(665)}}{a^*_{\text{phy}(665)}} \qquad \textit{Equation 12.}$$

With $a_{phy}^*(665)$ the chl *a* specific absorption coefficient at 665 nm. In the initial version of the algorithm, $a_{phy}^*(665)$ was calibrated using a variety of *in situ* measurements performed in inland and coastal waters (Gons *et al.*, 2002). Here, $a_{phy}^*(665)$ was estimated from field measurements performed during the bloom of *M. rubrum*. In practice, $a_{phy}^*(665)$ was determined as the slope of a linear fit between $a_{phy}(665)$ and chl *a* concentration, with $a_{phy}(665)$ retrieved from the *in situ* $R_{rs}(\lambda)$ measurements using equations 8-11. Finally, the fitted $a_{phy}^*(665)$ was compared to the range of bio-optical variability measured during the laboratory photoacclimation experiment.

Data analysis

Preliminary analysis of flow cytometry data was computed with the software MACSQuantify™ version 2.13.0 (Miltenyi Biotech). For the photoacclimation experiments, data analyses were performed with the R software, version 4.2.2 (R Core Team, 2022), with packages from the tidyverse project (Wickham *et al.*, 2019), and packages cmocean (Thyng *et al.*, 2016), ggpubr (Kassambara, 2023), reshape2 (Wickham, 2007) and viridis (Garnier *et al.*, 2023). With the exception of the atmospheric correction, the processing of satellite S2 data was performed using the Sentinel application platform (SNAP) software of the European Space Agency (ESA), version 9.0.0.

Results

Photoacclimation experiment

Different growth rates but similar light saturation in M. rubrum *and* T. amphioxeia

M. rubrum and *T. amphioxeia* were able to grow in culture over the investigated range of irradiance. For both species, growth rate was minimal at the lowest irradiance (20 µmol photons.m^{-2}.s^{-1}) and maximal at the highest irradiance (200 or 220 µmol photons.m^{-2}.s^{-1}). A fit with a Poisson function gives an estimate of the maximum growth rate (μ_m) and of the light saturation parameter for growth (K_E) which delimits the boundary between growth-limiting and growth-saturating irradiances (**Fig. 2A**). *T. amphioxeia* grew much faster than *M. rubrum* (μ_m=0.94 ± 0.04 d^{-1} in *T. amphioxeia* versus 0.47 ± 0.04 d^{-1} and 0.32 ± 0.01 d^{-1} in *M. rubrum* at 21 and 17.5°C, respectively) but showed similar K_E, suggesting similar adaptation to irradiance, although the precision of K_E estimation can be subject to caution regarding the few irradiance levels (3 to 4) used to fit the model. In terms of

volume, *M. rubrum* cells were about 100 times bigger than *T. amphioxeia* cells (**Fig. 2B**). Both cultures exhibited differences in cell biovolume, depending on irradiance and temperature. In particular, *M. rubrum* cells were smaller at low irradiances compared to 120 or 220 µmol photons.m^{-2}.s^{-1}, and generally smaller at 21°C compared to 17.5°C.

M. rubrum *photoacclimated pigment phenotypes are similar to those of its cryptophyte prey*

The analysis of lipophilic pigments by HPLC revealed the presence of the same pigments in both species, namely chl *a*, chl c_2, alloxanthin, β,ε-carotene, crocoxanthin and monadoxanthin, which are the typical lipophilic pigments of cryptophyte plastids (**Fig. 3, Fig. S2**). Minimal concentrations of pheopigments were detected in some cultures: pheophorbide *a* in *M. rubrum* cultures at 120 and 220 µmol photons.m^{-2}.s^{-1}; and pheophytin *a* in the same cultures and in all cultures of *T. amphioxeia* (**Fig. S2**). This indicates the degradation of chl *a* in these cultures, possibly due to the death of some cells. In the aqueous extracts of cultures, a single absorption peak at 552 nm with a shoulder at 565 nm was observed (**Fig. S3A**). This seems to confirm the presence of PE 545 as the only PBP in both species, though the maximum absorption wavelength showed a 7-nm offset. The slight offset between the observed (552 nm) *vs.* expected (545 nm) wavelength of the PE absorption maximum might result from a photoacclimation process occurring at the molecular level, in response to the spectral shape of the light field used to illuminate the cultures (Spangler *et al.*, 2022).

Pigment concentrations per cell biovolume were higher in *T. amphioxeia* than in *M. rubrum* at all irradiance levels, for chl *a*, chl c_2, alloxanthin and PE 545 (**Fig. 3**), consistent with the observed important space occupied by the chloroplast in the minute cell of *T. amphioxeia*, compared to the ciliate (**Fig. 1B and D**). Chl *a*, chl c_2 and alloxanthin concentrations decreased with irradiance in both species (**Fig**. **3A-C**). PE 545 cellular concentration showed a sharp decrease between 20 and 200 µmol photons.m^{-2}.s^{-1} in both species at 21°C (4.5-fold decrease for *T. amphioxeia* and 3-fold decrease for *M. rubrum*). For *M. rubrum* at 17.5°C however, only a small decrease at 220 µmol photons.m^{-2}.s^{-1} was observed (**Fig. 3D**). It is important to note that *M. rubrum* cultures at 17.5°C were sampled after a short period of photoacclimation (5 days), that corresponds to 1 to 2 generations given the observed growth rates. While the differences in pigment content between irradiance levels are already apparent, the cells in these cultures were still in the process of photoacclimation, and are not representative of fully acclimated phenotypes.

Absorption properties of **M. rubrum** *and* **T. amphioxeia** *show classical photoacclimation responses*

The absorption spectra of both species were almost identical in shape, consistent with the fact that the exact same pigments were identified in *M. rubrum* and *T. amphioxeia* (**Fig. S4**). For both

species, the spectral shape of the absorption coefficient was consistent with the presence of chl *a*, chl c_2, alloxanthin, and PE 545, with respective absorption peaks at 443 and 675, 460, 460 and 490, and 552 nm. The spectral signature of PE was only clearly visible when the absorption was measured from a suspension of living cells. When measured using the filter-pad technique, the absorption spectra lacked the characteristic peak of PE 545 (**Fig. 4**).

Cell absorption cross-section at 675 nm decreased sharply between 20 and 80 µmol photons.m^{-2}.s^{-1} in *T. amphioxeia* (-24%) and *M. rubrum* (-42%), followed by a much slighter decrease between 80 and 200 µmol photons.m^{-2}.s^{-1} (**Fig. 5A**). The chl *a*-specific absorption coefficient at 675 nm increased between the minimal and maximal irradiance levels, by 27% for *T. amphioxeia* and by 17% for *M. rubrum* (**Fig. 5B**). All values of a_p*(675) measured on cultures remained below the theoretical limit of absorption by chl *a* in seawater, $a_{sol,\text{chl }a}$*(675) = 0.0334 (Bricaud *et al.*, 2004), indicating some packaging effect in pigment absorption. For *T. amphioxeia*, a_p*(675) was higher than for *M. rubrum*, showing that the packaging effect was lower in the cryptophyte than in the ciliate. This is coherent with the theory of Morel and Bricaud (1981), which predicts that packaging effect is proportional to the size of the phytoplankton cell.

For both species at 21°C, absorption properties at 552 nm showed similar trends to those at 675 nm. σ_a(552) displayed a 48 and 62% decrease from 20 to 80 µmol photons.m^{-2}.s^{-1} in *M. rubrum* and *T. amphioxeia*, respectively, followed by a slighter decrease between 80 and 200 µmol photons.m^{-2}.s^{-1} in both species (**Fig. 5C**). Between 20 and 200 µmol photons.m^{-2}.s^{-1}, the phycoerythrin-specific absorption coefficient increased by 57% in *T. amphioxeia*. a_p*(552) was lower in *M. rubrum*, with similar values at 20 and 80 µmol photons.m^{-2}.s^{-1}, and a 27% increase at the highest irradiance level (**Fig. 5D**).

Comparison with field measurements and satellite remote sensing

M. rubrum *pigment composition in laboratory, field, and literature data*

We compared the accessory pigment/chl *a* ratios observed in our experiments with the results from a previous study (Rial *et al.*, 2013) in which *M. rubrum* was cultured at 2 irradiance levels (70 and 200 µmol photons.m^{-2}.s^{-1}). Overall, chl c_2/chl *a*, alloxanthin/chl *a* and β,ε-carotene/chl *a* ratios were comparable in both studies, though some differences emerge (**Fig. 6**). Rial *et al.* (2013) observed an increase of the chl *c2*/chl *a* ratio at high light compared to low light, no clear increase of the alloxanthin/chl *a* ratio with irradiance, and a β,ε-carotene/chl *a* ratio lower than in the present study. The results from the culture were also compared with that of field samples acquired during a bloom

of *M. rubrum* in Venezuela (Guzmán *et al.*, 2016) or in France (this study). Pigment/chl *a* ratios were very similar in both sampling locations. *In situ* samples showed chl c_2/chl *a* and β,ε-carotene/chl *a* ratios comparable to what was observed in cultures, but the alloxanthin/chl *a* ratio was markedly lower (**Fig. 6**), certainly because of the contribution of other phytoplankton taxa to the chl *a* biomass in natural environments. In samples from the 2021 *M. rubrum* bloom in France, pigments not specific to cryptophyte plastids were detected, namely fucoxanthin, peridinin and diadinoxanthin. This indicates that the bloom was not strictly monospecific, although largely dominated by *M. rubrum*. In particular, cells of the dinoflagellate *Scrippsiella sp.* were identified in preserved samples (Anne Schmitt, IFREMER LERMPL, Nantes, personal communication).

Optical characteristics and satellite remote sensing of a* M. rubrum *bloom

The particulate absorption coefficients measured *in vivo* (i.e., on suspended cells) was used as a reference to correct for pathlength amplification on filter pad measurements of corresponding cultures (Röttgers and Gehnke, 2012). It was compared with $a_p(\lambda)$ obtained using a generic correction proposed by Stramski *et al.* (2015) (**Suppl. Info. 1** and **Fig. S5A**). In the specific case of *M. rubrum* culture samples, the standard correction seems to overestimate $a_p(\lambda)$, with discrepancies increasing with the magnitude of absorption. However, when applied to the much lower absorption values from the bloom, the two corrections gave similar results. Compared to values of modelled $a_{phy}(665)$ obtained from the inversion of *in situ* reflectance, $a_{phy}(665)$ values measured with the filter pad technique are generally higher (more than twice higher for certain stations) regardless of which correction is applied. A linear regression of $a_{phy}(665)$ against the corresponding *in situ* [chl *a*] measured at each station led to several estimates of $a_{phy}^*(665)$ in the *M. rubrum* bloom (**Fig. S5B**), with important discrepancies between the two methods (*i.e.*, filter pad measurement or reflectance inversion) used for evaluating microalgal absorption in the bloom.

The linear regression of modelled $a_{phy}(665)$ versus [chl *a*] gives an estimated $a_{phy}^*(665)$ in the *M. rubrum* bloom of 0.0144 $m^2.mg_{chl\ a}^{-1}$ (adjusted $R^2 = 0.9046$, p-value < 0.001). This value is very close to the $a_{phy}^*(665) = 0.0146\ m^2.mg_{chl\ a}^{-1}$ determined by Gons *et al.* (2002) for a range of phytoplankton communities in coastal ecosystems. In contrast, using $a_{phy}(665)$ measured on filters leads to high estimations of $a_{phy}^*(665)$, close to or past the theoretical limit of the specific absorption coefficient of chl *a* in seawater at 665 nm (0.0217 $m^2.mg^{-1}$, Bricaud *et al.*, 2004). The potential reasons for this mismatch are discussed further in section 4.4 of this article. The value of $a_{phy}^*(665)$ determined from modelled $a_{phy}(665)$ was preferred for subsequent analyses, because it was closer to the values measured in the photoacclimation experiment and to the coefficient provided by Gons *et al.* (2002).

The values of a_{phy}*(665) for *M. rubrum* observed in this study range from 0.0071 $m^2.mg_{chl\ a}^{-1}$ (lowest value observed in culture) to 0.0144 $m^2.mg_{chl\ a}^{-1}$ (field measurements from the bloom) (**Fig. 7A**). The a_{phy}*(665) observed in the field is substantially higher than the highest measured in cultures of *M. rubrum* (0.0111 $m^2.mg_{chl\ a}^{-1}$). All these values are below the specific absorption coefficient of chl *a* in seawater, indicating some degree of package effect of chl *a* in *M. rubrum*. The sensitivity of the chl *a*-retrieval algorithm of Gons *et al.* (2002) to the choice of a_{phy}*(665) was illustrated by plotting [chl *a*] as a function of a_{phy}*(665), for 3 different values of a_{phy}(665) observed in the S2 image on 2021/03/27 (**Fig. 7B**). The values of a_{phy}*(665) represented in **Fig. 7A** are plotted as vertical lines, to illustrate the influence of the choice of one specific value of a_{phy}*(665) on the calculation of [chl *a*]. The percentage of variation of [chl *a*] depending on a_{phy}*(665) is independent of a_{phy}(665), but as [chl *a*] decreases exponentially when a_{phy}*(665) increases, the absolute variability is more important for higher values of a_{phy}(665) (**Supplementary table I**). This means that the uncertainty in remotely assessed [chl *a*] induced by different a_{phy}*(665) is maximized in the case of concentrated patches of microalgal blooms.

The value of a_{phy}*(665) determined *in situ* from the bloom samples was implemented into the algorithm of Gons *et al.* (2002) to create a map of [chl *a*] from the two Sentinel-2 images of the *M. rubrum* bloom on March 27 and 29, 2021 (**Fig. 8**). On March 27, [chl *a*] reached 250 $mg.m^{-3}$ in the most concentrated patches of the bloom. The distribution of chl *a* in the area was highly heterogenous, with concentrated patches of [chl *a*] > 100 $mg.m^{-3}$ forming narrow, filament-like structures approximately 50 to 150 m wide and 1.5 to 3 km long, surrounded by less-concentrated areas with [chl *a*] < 5 $mg.m^{-3}$ (**Fig. 8A**). On March 29, [chl *a*] was markedly lower throughout the area, with maxima around 40 $mg.m^{-3}$. The spatial extent of the bloom was visibly reduced compared to the previous image, with most patches close to the coastline (**Fig. 8B**).

Discussion

Biological and ecological implications of photoacclimation in M. rubrum *and* T. amphioxeia

Photoacclimation of pigment content in phytoplankton is a classic response to changes in irradiance, by which the rate of light absorption is fine-tuned to the energy needs of the cell (MacIntyre *et al.*, 2002). Modification of chl *a* content has been described in polar strains of *M. rubrum* (Johnson and Stoecker, 2005; Moeller *et al.*, 2011; Johnson *et al.*, 2023), but the response of the other pigments has largely been overlooked. To our knowledge, the only study that mentions the photoacclimation of phycoerythrin cellular content in this ciliate is that of Moeller *et al.* (2011). Our results show that temperate strains of *M. rubrum* also have the ability to photoacclimate. Moreover, we observed that

M. rubrum and *T. amphioxeia* pigment phenotypes display similar photoacclimation responses, where increasing irradiance is correlated with a decrease in the cellular content of all photosynthetic pigments (**Fig. 3, Fig. S2**). More specifically, the PE 545/chl *a* ratio shows a sharp decrease with increasing irradiance in both species (**Fig. S6**). This highlights the role of phycoerythrins in low-light environments in cryptophytes (Mendes *et al.*, 2023) and in their ciliate predator. Nevertheless, *M. rubrum* and its prey display differences in the mechanisms involved in photoacclimation. The most striking one is that photoacclimation in the cryptophytes *Teleaulax* and *Geminigera* is mediated by finely regulating the transcription of nucleus-encoded genes, while this light-dependent regulation is absent in the kleptokaryon of *M. rubrum* (Altenburger *et al.*, 2021; Johnson *et al.*, 2023). Given that the pigment phenotype of *M. rubrum* acclimates to changing light conditions, post-transcriptional processes are necessarily involved in the regulation of pigment synthesis, for both lipophilic pigments and phycobiliproteins. The evolutionary selection of such processes needed for photoacclimation in the ciliate can lead to two observations. First, it indicates that *M. rubrum* has reached a degree of specialization towards photosynthesis that seems unparalleled in other mixotrophic ciliates (Johnson *et al.*, 2023), and therefore occupies a peculiar trophic position among them as both a voracious (albeit specific) predator of nanophytoplankton and a significant contributor to primary production (Yih *et al.*, 2004; Johnson *et al.*, 2013). Second, it suggests that the ability to photoacclimate constitutes an important evolutionary bottleneck for planktonic organisms that rely on photosynthesis as their main trophic strategy, occurring in the early steps of permanent plastid acquisition.Six *et al.* (2021) demonstrated the key role that photosynthesis regulation and photoprotection play in the adaptation to cold or warm waters in marine cyanobacteria. The occurrence of *M. rubrum* across a wide range of latitudes (Dolan and Marrasé, 1995; van den Hoff and Bell, 2015) begs the question of the physiological and molecular adaptations of different strains to their respective environments, and of possible differences in photoacclimation responses between those strains. We should also note that “behavioural” adaptations, in association with photosynthesis regulation, probably play a significant role in the photophysiology of *M. rubrum*. Indeed, this highly motile organism seems to display irradiance-dependent phototaxis (Fenchel and Hansen, 2006), and performs important diel vertical migrations (Smith and Barber, 1979; Crawford, 1989). To what extent these migrations constitute an adaptation that maximizes photosynthetic growth and/or limits grazing pressure by predators remains in question.

One interesting aspect that our experiment did not control for is the importance of prey plastid photoacclimation for predator photophysiology, as the ciliates at all irradiance levels were fed with prey acclimated to low light (20 µmol photons.m^{-2}.s^{-1}). Considering the pigment concentrations in

high light-acclimated *M. rubrum* (200 µmol photons.m^{-2}.s^{-1}) and low light-acclimated *T. amphioxeia*, *M. rubrum* growth rate and the ingestion rate of *T. amphioxeia* cells by *M. rubrum*, we calculated that ingested prey pigments could contribute up to 22% of the total pigment content of *M. rubrum* (Suppl. Info. 2). While this is certainly a significant contribution, it means that the vast majority (> 78%) of the pigments are still directly produced *de novo* by *M. rubrum* cells, and that the observed photoacclimated phenotypes result mainly from ciliate metabolism. It is also worth noting that low light-acclimated cryptophytes that were added to high light environments likely experienced photooxidative stress, that the ciliate experienced as well after prey ingestion. This probably exerted an influence on the ciliate's physiology that we did not account for, but nevertheless highlights interesting questions regarding the importance of prey plastid photoacclimation in kleptoplastidic protists.

Variability of optical properties in **M. rubrum** *cultures and blooms*

Besides its implications in *M. rubrum* biology and ecology, photoacclimation can also play a role in the variability of seawater optical properties. It is widely recognized that phytoplankton are among the main drivers of optical variability in the surface ocean, with phytoplankton optical properties being influenced by changes in phytoplankton composition as well as by changes in the optical properties of individual cells of any species (Stramski *et al.*, 2001, 2002). In the case of massive blooms dominated by a single species, such as in *M. rubrum* red tides, optical variability primarily results from changes in the optical properties of individual cells of the dominant species. Here, we focused on changes in absorption cross-section and chl *a*-specific absorption, and how it can potentially influence estimation of [chl *a*] using satellite remote sensing (see 4.3).

In *T. amphioxeia* and *M. rubrum*, cell absorption cross-section was maximal at the lowest irradiance and minimal at the highest, while pigment-specific absorption coefficients (for both chl *a* and PE 545) followed an opposite trend (**Fig. 5**), a classical response for these parameters (MacIntyre *et al.*, 2002). We observe in particular that the *in vivo* absorption associated with PE 545 at 552 nm follows the same irradiance-dependent pattern as the absorption associated with chl *a* at 675 nm. This indicates that cryptophyte phycobiliproteins, although different in structure and localization from other photosynthetic pigments (including cyanobacterial and rhodophytan PBP), are submitted to similar bio-optical constraints, such as packaging effect.

The field measurements presented in this study show that the chl *a*-specific absorption of *M. rubrum* in the bloom is higher than that of cultures even at the highest irradiance, indicating a "high-light" acclimated phenotype. This may be explained in part by the aggregation of *M. rubrum*

in a thin layer near the surface, in an environment saturated with light (as observed and reviewed by Crawford, 1989). Moreover, phytoplankton phenotypes observed in the environment are generally less pigmented than their cultured counterparts (Graff *et al.*, 2016). This is mainly due to two factors: lower nutrient availability in natural environments limits growth and therefore the need for high energy acquisition and resource allocation to pigment synthesis; and highly variable natural light conditions favour phenotypes with fewer pigments. Although not explored in our work, nutrient availability probably exerts a major influence on the pigment phenotype and absorption properties of *M. rubrum*, as it has been observed in cryptophytes (Sciandra *et al.*, 2000). It is therefore very much possible that the pigment phenotypes of individual cells evolve with time, according to changes in light or nutrient availability, hence modifying the optical properties of the entire bloom. Additionally, seawater temperature measured on site shortly before the bloom (24 March 2021) was significantly lower (11.8°C; Quadrige Database, 2023) than those at which *M. rubrum* cells were cultivated in our experiments (17.5 and 21°C). As pigment content in phytoplankton generally decreases at lower temperatures (Hammer *et al.*, 2002), this can also contribute to the less-pigmented phenotype observed in the bloom.

Remote sensing of M. rubrum *blooms*

As previously mentioned, changes in the optical properties of individual cells can play a role in driving seawater optical variability in the case of red tides dominated by a given species. In particular, variability in the chl *a*-specific absorption coefficient is an important source of uncertainty in the estimation of [chl *a*] from satellite remote sensing, as a_{phy}*(665) is a key parameter in bio-optical algorithms based on reflectance inversion (Gons *et al.*, 2002; Bricaud *et al.*, 2004; Gilerson *et al.*, 2010; Zheng and DiGiacomo, 2017). For example, a recent study demonstrated that satellite measurement of [chl *a*] was improved when using a variable a_{phy}*(665) model rather than a fixed coefficient (Bramich *et al.*, 2021). The lab and field data presented here offer an opportunity to appraise the influence of photoacclimation-related changes in a_{phy}*(665) on the estimation of [chl *a*] by satellite remote sensing during a *M. rubrum* red tide. Although the lower values of the a_{phy}*(665) envelope correspond to extremely pigmented phenotypes that are less likely to occur in natural environments (Graff *et al.*, 2016), our results suggest that [chl *a*] retrieval can be underestimated by about 30% due to photoacclimation (Fig. 7D) if we consider the upper lab-measured a_{phy}*(665) as plausible.

The map of the bloom on 27 March 2021 (**Fig. 8A**) illustrates the spatial heterogeneity of *M. rubrum* blooms (Crawford, 1989), with patches of high [chl *a*] stretching in narrow filament-like

structures. These structures probably result mainly from hydrodynamics (Packard *et al.*, 1978), and to a lesser extent from the aggregation of the ciliates due to their motility. The map also shows important [chl *a*] reaching 250 $mg.m^{-3}$, highlighting the ability of *M. rubrum* blooms to reach high biomasses, although values four times higher have been observed (Smith and Barber, 1979). The second image on 29 March 2021 (**Fig. 8B**) shows the rapid evolution of the bloom during a short period of 2 days. The maximal [chl *a*] is drastically reduced, and the spatial distribution of the bloom greatly modified, with a few patches located closer to land. The rapid reduction in surface [chl *a*] observed in our study can be explained by a reduction in phytoplanktonic growth combined with increased losses. First, intra-specific competition for prey or nutrients may constitute a significant limitation to growth during the late stages of massive *M. rubrum* blooms, as starvation in ciliate populations rapidly leads to reduced growth rates (Kim *et al.*, 2017). Then, loss in ciliate biomass may have been caused by a combination of physical dispersal of the plankton by currents (both horizontal and vertical), migration of *M. rubrum* cells to deeper waters, and grazing by meso- or microzooplankton. Additionally, the role of parasites and viruses, that have been shown to exert strong control on phytoplankton populations (Chambouvet *et al.*, 2008; Biggs *et al.*, 2021), cannot be ruled out in the case of *M. rubrum* (Crawford *et al.*, 1997). Satellite remote sensing studies on the relation between local-scale hydrodynamics and the spatial structure of *M. rubrum* blooms, as well as field surveys of primary production and composition of the planktonic community during bloom events, would help elucidate the respective contributions of these phenomena to the bloom's distribution and decline.

Methodological bottlenecks and perspectives for the study of **M. rubrum** *in natural environments*

M. rubrum has sometimes been poorly represented in traditional surveys of planktonic communities, because of its rather confusing trophic position between phytoplankton and microzooplankton and of its fragility with regard to traditional methods of phytoplankton collection and preservation. Thus, its contribution to primary production has probably been underestimated in a number of studies (Crawford 1989). The pertinence of including *Mesodinium* as a genus of interest in field surveys has since been recognized, notably in the light of its trophic interaction with the toxic dinoflagellate *Dinophysis* (Harred and Campbell, 2014). In the absence of quantitative microscopic observation or imaging data, alloxanthin concentration (or alloxanthin/chl *a* ratio) can also be a good indicator of the presence or abundance of *M. rubrum*, although not self-sufficient as it is impossible to discriminate between *M. rubrum* and cryptophytes based on this pigment alone. Alloxanthin is the specific pigment of cryptophytes, used in CHEMTAX analyses to assess the contribution of cryptophytes to the phytoplankton biomass. As noted by Llewellyn *et al.* (2005),

seasonal *M. rubrum* blooms could periodically constitute a significant part of the cryptophyte-chl *a* inferred from such methods. Inversely, the similarity in pigment content and optical properties means that cryptophyte red tides observed on satellite images could also be misidentified as *M. rubrum*. This highlights the importance of confirming the identity of the causative organism of a red tide (via microscopic observation) whenever possible.

Phycoerythrin 545 is even more specific to *M. rubrum* and its cryptophyte prey, as it is only produced by certain cryptophyte genera, including those upon which *M. rubrum* acquires its plastids (Altenburger *et al.*, 2020). Despite this, PE 545 has rarely been measured when studying the pigments of *M. rubrum* (Rial *et al.*, 2013; Gaillard *et al.*, 2020), especially when it comes to field studies (Dierssen *et al.*, 2015; Guzmán *et al.*, 2016; this study). Indeed, this protein presents a series of constraints and limitations for its accurate quantification. First, due to its hydrophilic nature, it is not extracted and eluted along the chlorophylls and carotenoids, and hence not measured with classical HPLC protocols. It is therefore necessary to collect extra samples specifically for this pigment. However, as was demonstrated by Lawrenz *et al.* (2011) and confirmed by experiments conducted by us prior to this study (**Fig. S3**), it is not possible to efficiently recover phycobiliproteins from samples filtered on glass fiber filters, contrary to lipophilic pigments. This could be due to a strong binding of phycobiliproteins with the glass fibers, preventing any further extraction in aqueous solvents. This hypothesis is supported by the fact that PE 545 is visibly present on GF/F filters, that show a bright pink coloration on the back side, but cannot be extracted (**Fig. S3**). This also poses a problem for the analysis of absorption spectra with the filter-pad technique, as the specific absorption peak of PE 545 is significantly reduced (**Fig. 4**).

Moreover, the traditional filter pad technique seems to reach some limits when it comes to precise measurements of specific absorption coefficients. Measurements of microalgal absorption performed using filter pads often give strangely high a_{phy}*(665) values, as noted by Zheng and DiGiacomo (2017). This was also the case in our study, with measurements of a_{phy}*(665) flirting with or going beyond the theoretical limit of absorption of dissolved chl *a* in seawater (**Fig. S5B**). While Zheng and DiGiacomo (2017) mention that the absorption of chlorophyll *b* at 665 nm could contribute to these high a_{phy}*(665) values, HPLC analysis of our bloom samples did not reveal any chl *b*, ruling this explanation out. Bricaud *et al.* (2004) discussed a similar phenomenon with the chl *a*-specific absorption coefficient at 440 nm they observed in many samples from various oceanographic cruises. The mismatch between the absorption values measured with filter pads or modelled from *in situ* reflectance in our study also illustrates the apparent overestimation of absorption occurring with the filter pad technique. While the explanations for this phenomenon remain unclear, we argue that this uncertainty in absorption measurements is problematic, in

particular as more *in situ* measurements of *M. rubrum* blooms are needed to better characterize the range of absorption properties of this ciliate in different environments.

Methods for studying *M. rubrum* blooms in the field should take these considerations into account, as well as adapt to the peculiarities of phycobiliproteins and to the fragility of the ciliate. For absorption measurements, non-destructive methods should be preferred whenever possible. For example, using a point-source integrating-cavity absorption meter (PSICAM, Röttgers *et al.*, 2007) for near *in situ* measurements could be promising, as this device is adapted to the relatively low cell densities in the field and overcomes the measurement issues caused by glass fiber filters. To collect samples for PE 545 measurements, concentrating the algal biomass by filtering seawater on hydrophobic polycarbonate filters could be envisioned, though this method still needs to be thoroughly tested. Another option would be to sample relatively small volumes of seawater for centrifugation and quantify PE 545 through fluorescence measurement rather than absorption, as the former is much more sensitive and requires less biomass. Such a protocol would nonetheless require prior appropriate calibration.

The importance of PE 545 for *M. rubrum* ecophysiology should motivate such investigations towards measurements in natural environments. Moreover, this pigment is responsible for the characteristic shape of the reflectance spectrum of *M. rubrum* blooms, with low reflectance in the green spectral region (Gernez *et al.*, 2023). Knowledge about PE 545 optical properties *in situ* is therefore determinant for developing remote-sensing algorithms designed to accurately detect and characterize *M. rubrum* blooms. High resolution satellite remote sensing is indeed a promising tool for studying these periodical, ecologically important phenomena in coastal waters (Dierssen *et al.*, 2015; Gernez *et al.*, 2023).

Conclusions

The kleptoplastidic ciliate *M. rubrum* shows classical photoacclimation responses similar to that of its cryptophyte prey. Different pigment phenotypes in *M. rubrum* induce variability in its absorption properties, including the chl *a*-specific absorption coefficient that is used in chl *a*-estimation algorithms from remote sensing reflectance. High resolution satellite remote sensing of a coastal red tide shows that *M. rubrum* forms concentrated patches of cells that stretch over several kilometers, and that the spatial structure and chl *a* biomass of the bloom change rapidly over a short period of 2 days. Overall, these results shed light on the ecophysiology of *M. rubrum*, a peculiar mixotrophic ciliate with a high degree of specialization towards photosynthesis. Future studies will have to

overcome technical challenges to better characterize the physiology and pigment composition of this ecologically important ciliate during blooms in natural environments.

Acknowledgements

We are grateful to Dr. David Jaén (LCCRRPP, Junta de Andalucía, Spain) for generously sharing his cultures of *Teleaulax amphioxeia* (AND-A0710) and to Dr. Per Juel Hansen (marine Biological Station, University of Copenhagen, Helsingør, Denmark) for his strain of *Mesodinium rubrum* (MrDK-2009). We sincerely thank Florian Massuyeau (Institut des Matériaux-Jean Rouxel, Nantes Université, France) for letting us use the dual beam UV-Vis-NIR spectrophotometer at his institute, and for helping us with measurements. Thank you to Aurélie Charrier, Virginie Raimbault, Marie Engel and Léna Gouhier (PHYTOX Physalg, IFREMER Nantes) for their help during culture work, and Elise Robert (PHYTOX Genalg, IFREMER Nantes) for pigment analysis. We sincerely thank Christophe Six and Sarah Garric of the Roscoff Biological Station for their helpful insights and comments on a previous version of this work. We thank two anonymous reviewers for their critical and relevant comments on the first version of this manuscript. Finally, we thank the French taxpayers for supporting this research through our salaries and public funding of project LASHA (CNES).

Funding

This work was supported by the Centre National d'Etudes Spatiales (CNES, France) during the TOSCA project LAboratory to Satellite experiments for remote sensing of Harmful Algae (LASHA).

Data Archiving

A github repository with all the R scripts used to analyse data presented in this study, as well as the associated raw data, is available at https://github.com/vpochic/photoacclim2.0. Data absent from the repository (satellite images) are available upon request.

References

Altenburger, A., Blossom, H. E., Garcia-Cuetos, L., Jakobsen, H. H., Carstensen, J., Lundholm, N., Hansen, P. J., Moestrup, Ø., *et al.* (2020) Dimorphism in cryptophytes—The case of *Teleaulax amphioxeia*/*Plagioselmis prolonga* and its ecological implications. *Sci. Adv.*, **6**, eabb1611. https://doi.org/10.1126/sciadv.abb1611

Altenburger, A., Cai, H., Li, Q., Drumm, K., Kim, M., Zhu, Y., Garcia-Cuetos, L., Zhan, X., *et al.* (2021) Limits to the cellular control of sequestered cryptophyte prey in the marine ciliate *Mesodinium rubrum*. *ISME J.*, **15**, 1056–1072. https://doi.org/10.1038/s41396-020-00830-9

Barber, R. T., White, A. W., and Siegelman, H. W. (1969). Evidence for a cryptomonad symbiont in the ciliate, *Cyclotrichium meunieri*. *J. Phycol.*, **5**, 86-88. https://doi.org/10.1111/j.1529-8817.1969.tb02583.x

Biggs, T. E. G., Huisman, J., and Brussaard, C. P. D. (2021) Viral lysis modifies seasonal phytoplankton dynamics and carbon flow in the Southern Ocean. *ISME J.*, **15**, 3615–3622. https://doi.org/10.1038/s41396-021-01033-6

Bramich, J., Bolch, C. J., and Fischer, A. (2021). Improved red-edge chlorophyll-*a* detection for Sentinel 2. *Ecol. Indic.*, **120**, 106876. https://doi.org/10.1016/j.ecolind.2020.106876

Bricaud, A. and Stramski, D. (1990) Spectral absorption coefficients of living phytoplankton and nonalgal biogenous matter: A comparison between the Peru upwelling area and the Sargasso Sea. *Limnol. Oceanogr.*, **35**, 562–582. https://doi.org/10.4319/lo.1990.35.3.0562

Bricaud, A., Babin, M., Morel, A., and Claustre, H. (1995) Variability in the chlorophyll-specific absorption coefficients of natural phytoplankton: Analysis and parameterization. *J. Geophys. Res.: Oceans*, **100**, 13321–13332. https://doi.org/10.1029/95JC00463

Bricaud, A., Claustre, H., Ras, J., and Oubelkheir, K. (2004) Natural variability of phytoplanktonic absorption in oceanic waters: Influence of the size structure of algal populations. *J. Geophys. Res.: Oceans*, **109**. https://doi.org/10.1029/2004JC002419

Caballero, I., Fernández, R., Escalante, O. M., Mamán, L., and Navarro, G. (2020) New capabilities of Sentinel-2A/B satellites combined with in situ data for monitoring small harmful algal blooms in complex coastal waters. *Sci. Rep.*, **10**, 8743. https://doi.org/10.1038/s41598-020-65600-1

Chambouvet, A., Morin, P., Marie, D., and Guillou, L. (2008) Control of Toxic Marine Dinoflagellate Blooms by Serial Parasitic Killers. *Science*, **322**, 1254–1257. https://doi.org/10.1126/science.1164387

Craig, S. E., Lohrenz, S. E., Lee, Z., Mahoney, K. L., Kirkpatrick, G. J., Schofield, O. M., and Steward, R. G. (2006) Use of hyperspectral remote sensing reflectance for detection and assessment of the harmful alga, *Karenia brevis*. *Appl. Opt.*, AO, **45**, 5414–5425. https://doi.org/10.1364/AO.45.005414

Crawford, D. (1989) *Mesodinium rubrum*: the phytoplankter that wasn't. *Mar. Ecol.: Prog. Ser.*, **58**, 161–174. https://doi.org/10.3354/meps058161

Crawford, D. W., Purdie, D. A., Lockwood, A. P. M., and Weissman, P. (1997) Recurrent Red-tides in the Southampton Water Estuary Caused by the Phototrophic Ciliate *Mesodinium rubrum*. *Estuarine, Coastal Shelf Sci.*, **45**, 799–812. https://doi.org/10.1006/ecss.1997.0242

Cunningham, B. R., Greenwold, M. J., Lachenmyer, E. M., Heidenreich, K. M., Davis, A. C., Dudycha, J. L., and Richardson, T. L. (2019) Light capture and pigment diversity in marine and freshwater cryptophytes. *J. Phycol.*, **55**, 552–564. https://doi.org/10.1111/jpy.12816

Darwin, C. (1839) Voyage of the Beagle. Penguin Books, London.

Denman, K. L. and Gargett, A. E. (1983) Time and space scales of vertical mixing and advection of phytoplankton in the upper ocean. *Limnol. Oceanogr.*, **28**, 801–815. https://doi.org/10.4319/lo.1983.28.5.0801

Díaz, P. A., Ruiz-Villarreal, M., Mouriño-Carballido, B., Fernández-Pena, C., Riobó, P., and Reguera, B. (2019) Fine scale physical-biological interactions during a shift from relaxation to upwelling with a focus on *Dinophysis acuminata* and its potential ciliate prey. *Prog. Oceanogr.*, **175**, 309–327. https://doi.org/10.1016/j.pocean.2019.04.009

740 Dierssen, H., McManus, G. B., Chlus, A., Qiu, D., Gao, B.-C., and Lin, S. (2015) Space station
741 image captures a red tide ciliate bloom at high spectral and spatial resolution. *Proc. Natl.*
742 *Acad. Sci. U. S. A.*, **112**, 14783–14787. https://doi.org/10.1073/Proc. Natl. Acad. Sci. U. S.
743 A..1512538112
744
745 Dolan, J. R. and Marrasé, C. (1995) Planktonic ciliate distribution relative to a deep chlorophyll
746 maximum: Catalan Sea, N.W. Mediterranean, June 1993. *Deep Sea Res., Part I*, **42**, 1965–
747 1987. https://doi.org/10.1016/0967-0637(95)00092-5
748
749 Doust, A. B., Marai, C. N. J., Harrop, S. J., Wilk, K. E., Curmi, P. M. G., and Scholes, G. D. (2004)
750 Developing a Structure–Function Model for the Cryptophyte Phycoerythrin 545 Using
751 Ultrahigh Resolution Crystallography and Ultrafast Laser Spectroscopy. *J. Mol. Biol.*, **344**,
752 135–153. https://doi.org/10.1016/j.jmb.2004.09.044
753
754 Fenchel, T. and Hansen, P. J. (2006) Motile behaviour of the bloom-forming ciliate *Mesodinium*
755 *rubrum*. *Mar. Biol. Res.*, **2**, 33–40. https://doi.org/10.1080/17451000600571044
756
757 Gaillard, S., Charrier, A., Malo, F., Carpentier, L., Bougaran, G., Hégaret, H., Réveillon, D., Hess,
758 P., *et al.* (2020) Combined Effects of Temperature, Irradiance, and pH on *Teleaulax*
759 *amphioxeia* (Cryptophyceae) Physiology and Feeding Ratio For Its Predator *Mesodinium*
760 *rubrum* (Ciliophora)1. *J. Phycol.*, **56**, 775–783. https://doi.org/10.1111/jpy.12977
761
762 Garnier, S., Ross, N., Rudis, R., Camargo, P. A., Sciaini, M., Scherer, C. (2023) viridis(Lite) -
763 Colorblind-Friendly Color Maps for R. doi:10.5281/zenodo.4678327, viridisLite package
764 version 0.4.2, https://sjmgarnier.github.io/viridis/.
765
766 Gernez, P., Doxaran, D., and Barillé, L. (2017) Shellfish Aquaculture from Space: Potential of
767 Sentinel2 to Monitor Tide-Driven Changes in Turbidity, Chlorophyll Concentration and
768 Oyster Physiological Response at the Scale of an Oyster Farm. *Front. Mar. Sci.*, **4**.
769 https://doi.org/10.3389/fmars.2017.00137
770

771 Gernez, P., Zoffoli, M. L., Lacour, T., Hernandez Fariñas, T., Navarro, G., Caballero, I., and
772 Harmel, T. (2023) The many shades of red tides: Sentinel-2 optical types of highly-
773 concentrated harmful algal blooms. *Remote Sens. Environ.*, **287**, 113486.
774 https://doi.org/10.1016/j.rse.2023.113486
775
776 Gilerson, A. A., Gitelson, A. A., Zhou, J., Gurlin, D., Moses, W., Ioannou, I., and Ahmed, S. A.
777 (2010) Algorithms for remote estimation of chlorophyll-*a* in coastal and inland waters using
778 red and near infrared bands. *Opt. Express, OE*, **18**, 24109–24125.
779 https://doi.org/10.1364/OE.18.024109
780
781 Gomori, G. (1955) [16] Preparation of buffers for use in enzyme studies. Methods in Enzymology.
782 Academic Press, pp. 138–146.
783
784 Gons, H. J. (1999) Optical Teledetection of Chlorophyll *a* in Turbid Inland Waters. *Environ. Sci.*
785 *Technol.*, **33**, 1127–1132. https://doi.org/10.1021/es9809657
786
787 Gons, H. J., Rijkeboer, M., and Ruddick, K. G. (2002) A chlorophyll-retrieval algorithm for
788 satellite imagery (Medium Resolution Imaging Spectrometer) of inland and coastal waters.
789 *J. Plankton Res.*, **24**, 947–951. https://doi.org/10.1093/plankt/24.9.947
790
791 Graff, J. R., Westberry, T. K., Milligan, A. J., Brown, M. B., Dall'Olmo, G., Reifel, K. M., and
792 Behrenfeld, M. J. (2016) Photoacclimation of natural phytoplankton communities. *Mar.*
793 *Ecol.: Prog. Ser.*, **542**, 51–62. https://doi.org/10.3354/meps11539
794
795 Guillard, R. R. L. and Hargraves, P. E. (1993) *Stichochrysis immobilis* is a diatom, not a
796 chrysophyte. *Phycologia*, **32**, 234-236. https://doi.org/10.2216/i0031-8884-32-3-234.1
797
798 Guillotreau, P., Bihan, V. L., Morineau, B., and Pardo, S. (2021) The vulnerability of shellfish
799 farmers to HAB events: An optimal matching analysis of closure decrees. *Harmful Algae*,
800 **101**, 101968. https://doi.org/10.1016/j.hal.2020.101968
801

802 Gustafson, D. E., Stoecker, D. K., Johnson, M. D., Van Heukelem, W. F., and Sneider, K. (2000)
803 Cryptophyte algae are robbed of their organelles by the marine ciliate *Mesodinium rubrum*.
804 *Nature*, **405**, 1049–1052. https://doi.org/10.1038/35016570
805
806 Guzmán, L., Varela, R., Muller-Karger, F., and Lorenzoni, L. (2016) Bio-optical characteristics of a
807 red tide induced by *Mesodinium rubrum* in the Cariaco Basin, Venezuela. *J. Marine Syst.*, **160**, 17–
808 25. https://doi.org/10.1016/j.jmarsys.2016.03.015
809 Hammer, A., Schumann, R., and Schubert, H. (2002) Light and temperature of *Rhodomonas salina*
810 (Cryptophyceae): photosynthetic performance. *Aquat. Microb. Ecol.*, **29**, 287–296.
811 https://doi.org/10.3354/ame029287
812
813 Harmel, T., Chami, M., Tormos, T., Reynaud, N., and Danis, P.-A. (2018) Sunglint correction of
814 the Multi-Spectral Instrument (MSI)-SENTINEL-2 imagery over inland and sea waters from
815 SWIR bands. *Remote Sens. Environ.*, **204**, 308–321.
816 https://doi.org/10.1016/j.rse.2017.10.022
817
818 Harred, L. B. and Campbell, L. (2014) Predicting harmful algal blooms: a case study with
819 *Dinophysis ovum* in the Gulf of Mexico. *J. Plankton Res.*, **36**, 1434–1445.
820 https://doi.org/10.1093/plankt/fbu070
821
822 Hart, T. J. (1943) Darwin and 'Water-Bloom'. *Nature*, **152**, 661–662.
823 https://doi.org/10.1038/152661b0
824
825 Heidenreich, K. M. and Richardson, T. L. (2020) Photopigment, Absorption, and Growth
826 Responses of Marine Cryptophytes to Varying Spectral Irradiance. *J. Phycol.*, **56**, 507–520.
827 https://doi.org/10.1111/jpy.12962
828
829 Hernández-Urcera, J., Rial, P., García-Portela, M., Lourés, P., Kilcoyne, J., Rodríguez, F.,
830 Fernández-Villamarín, A., and Reguera, B. (2018) Notes on the Cultivation of Two
831 Mixotrophic *Dinophysis* Species and Their Ciliate Prey *Mesodinium rubrum*. *Toxins*, **10**,
832 505. https://doi.org/10.3390/toxins10120505
833

834 Jaubert, M., Bouly, J.-P., Ribera d'Alcalà, M., and Falciatore, A. (2017) Light sensing and
835 responses in marine microalgae. *Curr. Opin. Plant. Biol.*, **37**, 70–77.
836 https://doi.org/10.1016/j.pbi.2017.03.005
837
838 Johnson, M. D., Moeller, H. V., Paight, C., Kellogg, R. M., McIlvin, M. R., Saito, M. A., and
839 Lasek-Nesselquist, E. (2023) Functional control and metabolic integration of stolen
840 organelles in a photosynthetic ciliate. *Curr. Biol.*, **33**, 973-980.e5.
841 https://doi.org/10.1016/j.cub.2023.01.027
842
843 Johnson, M. D. and Stoecker, D. K. (2005) Role of feeding in growth and photophysiology of
844 *Myrionecta rubra*. *Aquat. Microb. Ecol.*, **39**, 303–312. https://doi.org/10.3354/ame039303
845
846 Johnson, M. D., Stoecker, D. K., and Marshall, H. G. (2013) Seasonal dynamics of *Mesodinium*
847 *rubrum* in Chesapeake Bay. *J. Plankton Res.*, **35**, 877–893.
848 https://doi.org/10.1093/plankt/fbt028
849
850 Kassambara, A. (2023) ggpubr: 'ggplot2' Based Publication Ready Plots. R package version 0.6.0,
851 https://rpkgs.datanovia.com/ggpubr/
852
853 Kim, M., Drumm, K., Daugbjerg, N., and Hansen, P. J. (2017) Dynamics of Sequestered
854 Cryptophyte Nuclei in *Mesodinium rubrum* during Starvation and Refeeding. *Front.*
855 *Microbiol.*, **8**. https://doi.org/10.3389/fmicb.2017.00423
856
857 Lacour, L., Ardyna, M., Stec, K. F., Claustre, H., Prieur, L., Poteau, A., Ribera d'Alcala, M., and
858 Iudicone, D. (2017) Unexpected winter phytoplankton blooms in the North Atlantic
859 subpolar gyre. *Nat. Geosci.*, **10**, 836–839. https://doi.org/10.1038/ngeo3035
860
861 Laviale, M. and Neveux, J. (2011) Relationships between pigment ratios and growth irradiance in
862 11 marine phytoplankton species. *Mar. Ecol.: Prog. Ser.*, **425**, 63–77.
863 https://doi.org/10.3354/meps09013
864

865 Lawrenz, E., Fedewa, E. J., and Richardson, T. L. (2011) Extraction protocols for the quantification
866 of phycobilins in aqueous phytoplankton extracts. *J. Appl. Phycol.*, **23**, 865–871.
867 https://doi.org/10.1007/s10811-010-9600-0
868
869 Leong, S. C. Y. and Taguchi, S. (2006) Detecting the bloom-forming dinoflagellate *Alexandrium*
870 *tamarense* using the absorption signature. *Hydrobiologia*, **568**, 299–308.
871 https://doi.org/10.1007/s10750-006-0202-4
872
873 Llewellyn, C. A., Fishwick, J. R., and Blackford, J. C. (2005) Phytoplankton community
874 assemblage in the English Channel: a comparison using chlorophyll *a* derived from HPLC-
875 CHEMTAX and carbon derived from microscopy cell counts. *J. Plankton Res.*, **27**, 103–
876 119. https://doi.org/10.1093/plankt/fbh158
877
878 MacColl, R., Berns, D. S., and Gibbons, O. (1976) Characterization of cryptomonad phycoerythrin
879 and phycocyanin. *Arch. Biochem. Biophys.*, **177**, 265–275. https://doi.org/10.1016/0003-
880 9861(76)90436-7
881
882 MacIntyre, H. L., Kana, T. M., Anning, T., and Geider, R. J. (2002) Photoacclimation of
883 Photosynthesis Irradiance Response Curves and Photosynthetic Pigments in Microalgae and
884 Cyanobacteria. *J. Phycol.*, **38**, 17–38. https://doi.org/10.1046/j.1529-8817.2002.00094.x
885
886 Mafra, L. L., Nolli, P. K. W., Mota, L. E., Domit, C., Soeth, M., Luz, L. F. G., Sobrinho, B. F.,
887 Leal, J. G., *et al.* (2019) Multi-species okadaic acid contamination and human poisoning
888 during a massive bloom of *Dinophysis acuminata* complex in southern Brazil. *Harmful*
889 *Algae*, **89**, 101662. https://doi.org/10.1016/j.hal.2019.101662
890
891 Mendes, C. R. B., Costa, R. R., Ferreira, A., Jesus, B., Tavano, V. M., Dotto, T. S., Leal, M. C.,
892 Kerr, R., *et al.* (2023) Cryptophytes: An emerging algal group in the rapidly changing
893 Antarctic Peninsula marine environments. *Glob. Change Biol.*, **29**, 1791–1808.
894 https://doi.org/10.1111/gcb.16602
895

Minnhagen, S., Kim, M., Salomon, P. S., Yih, W., Granéli, E., and Park, M. G. (2011) Active uptake of kleptoplastids by *Dinophysis caudata* from its ciliate prey *Myrionecta rubra*. *Aquat. Microb. Ecol.*, **62**, 99–108. https://doi.org/10.3354/ame01459

Moeller, H. V., Johnson, M. D., and Falkowski, P. G. (2011) Photoacclimation in the Phototrophic Marine Ciliate *Mesodinium rubrum* (Ciliophora). *J. Phycol.*, **47**, 324–332. https://doi.org/10.1111/j.1529-8817.2010.00954.x

Morel, A. and Bricaud, A. (1981) Theoretical results concerning light absorption in a discrete medium, and application to specific absorption of phytoplankton. *Deep Sea Res.*, **28**, 1375–1393. https://doi.org/10.1016/0198-0149(81)90039-X

Morel, A. and Prieur, L. (1977) Analysis of variations in ocean color. *Limnol. Oceanogr.*, **22**, 709–722. https://doi.org/10.4319/lo.1977.22.4.0709

Mueller, J. L. (2003) In-Water Radiometric Profile Measurements and Data Analysis Protocols. In Fargion, G. S., McClain, C. R. and Mueller, J. L. (eds), *Ocean Optics Protocols for Satellite Ocean Color Sensor Validation, Revision 4. Volume III: Radiometric Measurements and Data Analysis Protocols*. National Aeronautics and Space Administration, Goddard Space Flight Center https://doi.org/10.25607/OBP-62

Overkamp, K. E., Gasper, R., Kock, K., Herrmann, C., Hofmann, E., and Frankenberg-Dinkel, N. (2014) Insights into the Biosynthesis and Assembly of Cryptophycean Phycobiliproteins. *J. Biol. Chem.*, **289**, 26691–26707. https://doi.org/10.1074/jbc.M114.591131

Packard, T. T., Blasco, D., and Barber, R. T. (1978) *Mesodinium rubrum* in the Baja California Upwelling System. In Boje, R. and Tomczak, M. (eds), *Upwelling Ecosystems*. Springer, Berlin, Heidelberg, pp. 73–89. https://doi.org/10.1007/978-3-642-66985-9_7

Park, M. G., Kim, S., Kim, H. S., Myung, G., Kang, Y. G., and Yih, W. (2006) First successful culture of the marine dinoflagellate *Dinophysis acuminata*. *Aquat. Microb. Ecol.*, **45**, 101–106. https://doi.org/10.3354/ame045101

928

929 Peltomaa, E. and Johnson, M. D. (2017) *Mesodinium rubrum* exhibits genus-level but not species-
930 level cryptophyte prey selection. *Aquat. Microb. Ecol.*, **78**, 147–159.
931 https://doi.org/10.3354/ame01809
932

933 Quadrige (2023). Données par paramètre. Quadrige (Ifremer). https://doi.org/10.12770/cf5048f6-
934 5bbf-4e44-ba74-e6f429af51ea
935

936 R Core Team (2022). R: A language and environment for statistical computing. R Foundation for
937 Statistical Computing, Vienna, Austria. URL https://www.R-project.org/
938

939 Rial, P., Garrido, J. L., Jaén, D., and Rodríguez, F. (2013) Pigment composition in three *Dinophysis*
940 species (Dinophyceae) and the associated cultures of *Mesodinium rubrum* and *Teleaulax*
941 *amphioxeia*. *J. Plankton Res.*, **35**, 433–437. https://doi.org/10.1093/plankt/fbs099
942

943 Richardson, T. L. (2022) The colorful world of cryptophyte phycobiliproteins. *J. Plankton Res.*, **44**,
944 806–818. https://doi.org/10.1093/plankt/fbac048
945

946 Roesler, C., Stramski, D., D'Sa, E. J., Röttgers, R., and Reynolds, R. A. (2018) Chapter 5:
947 Spectrophotometric Measurements of Particulate Absorption Using Filter Pads. In Neeley,
948 A. R. and Mannino, A. (eds), *IOCCG Protocol Series (2018). Inherent Optical Property*
949 *Measurements and Protocols: Absorption Coefficient*, IOCCG Ocean Optics and
950 Biogeochemistry Protocols for Satellite Ocean Colour Sensor Validation. Dartmouth, NS,
951 Canada. http://dx.doi.org/10.25607/OBP-119
952

953 Röttgers, R. and Gehnke, S. (2012) Measurement of light absorption by aquatic particles:
954 improvement of the quantitative filter technique by use of an integrating sphere approach.
955 *Appl. Opt., AO*, **51**, 1336–1351. https://doi.org/10.1364/AO.51.001336
956

957 Röttgers, R., Häse, C., and Doerffer, R. (2007) Determination of the particulate absorption of
958 microalgae using a point-source integrating-cavity absorption meter: verification with a

959 photometric technique, improvements for pigment bleaching, and correction for chlorophyll
960 fluorescence. *Limnol. Oceanogr. Meth.*, **5**, 1–12. https://doi.org/10.4319/lom.2007.5.1
961
962 Ruddick, K. G., De Cauwer, V., Park, Y.-J., and Moore, G. (2006) Seaborne measurements of near
963 infrared water-leaving reflectance: The similarity spectrum for turbid waters. *Limnol.*
964 *Oceanogr.*, **51**, 1167–1179. https://doi.org/10.4319/lo.2006.51.2.1167
965
966 Sciandra, A., Lazzara, L., Claustre, H., and Babin, M. (2000) Responses of growth rate, pigment
967 composition and optical properties of *Cryptomonas sp.* to light and nitrogen stresses. *Mar.*
968 *Ecol.: Prog. Ser.*, **201**, 107–120. https://doi.org/10.3354/meps201107
969
970 Six, C., Ratin, M., Marie, D. and Corre, E. (2021) Marine *Synechococcus* picocyanobacteria: Light
971 utilization across latitudes. *Proc. Natl. Acad. Sci. USA*, **118**, e2111300118.
972 https://doi.org/10.1073/pnas.21113001
973
974 Smith, W. O. Jr. and Barber, R. T. (1979) A Carbon Budget for the Autotrophic Ciliate *Mesodinium*
975 *rubrum*. *J. Phycol.*, **15**, 27–33. https://doi.org/10.1111/j.1529-8817.1979.tb02957.x
976
977 Spangler, L. C., Yu, M., Jeffrey, P. D., and Scholes, G. D. (2022) Controllable Phycobilin
978 Modification: An Alternative Photoacclimation Response in Cryptophyte Algae. *ACS Cent.*
979 *Sci.*, **8**, 340–350. https://doi.org/10.1021/acscentsci.1c01209
980
981 Stramski, D., Bricaud, A., and Morel, A. (2001) Modeling the inherent optical properties of the
982 ocean based on the detailed composition of the planktonic community. *Appl. Opt., AO*, **40**,
983 2929–2945. https://doi.org/10.1364/AO.40.002929
984
985 Stramski, D. and Mobley, C. D. (1997) Effects of microbial particles on oceanic optics: A database
986 of single-particle optical properties. *Limnol. Oceanogr.*, **42**, 538–549.
987 https://doi.org/10.4319/lo.1997.42.3.0538
988
989 Stramski, D., Reynolds, R. A., Kaczmarek, S., Uitz, J., and Zheng, G. (2015) Correction of
990 pathlength amplification in the filter-pad technique for measurements of particulate

absorption coefficient in the visible spectral region. *Appl. Opt.*, AO, **54**, 6763–6782. https://doi.org/10.1364/AO.54.006763

Stramski, D., Rosenberg, G., and Legendre, L. (1993) Photosynthetic and optical properties of the marine chlorophyte *Dunaliella tertiolecta* grown under fluctuating light caused by surface-wave focusing. *Marine Biology*, **115**, 363–372. https://doi.org/10.1007/BF00349833

Stramski, D., Sciandra, A., and Claustre, H. (2002) Effects of temperature, nitrogen, and light limitation on the optical properties of the marine diatom *Thalassiosira pseudonana*. *Limnol. Oceanogr.*, **47**, 392–403. https://doi.org/10.4319/lo.2002.47.2.0392

Thyng, K. M., Greene, C. A., Hetland, R. D., Zimmerle, H. M., and DiMarco, S. F. (2016) True Colors of Oceanography: Guidelines for Effective and Accurate Colormap Selection. *Oceanography*, **29**, 9–13. https://doi.org/10.5670/oceanog.2016.66

van den Hoff, J. and Bell, E. (2015) The ciliate *Mesodinium rubrum* and its cryptophyte prey in Antarctic aquatic environments. *Polar Biol.*, **38**, 1305–1310. https://doi.org/10.1007/s00300-015-1686-z

Wickham, H. (2007) Reshaping Data with the reshape Package. *J. Stat. Softw.*, **21**, 1–20. https://doi.org/10.18637/jss.v021.i12

Wickham, H., Averick, M., Bryan, J., Chang, W., McGowan, L. D., François, R., Grolemund, G., Hayes, A., *et al.* (2019) Welcome to the Tidyverse. *Journal of Open Source Software*, **4**, 1686. https://doi.org/10.21105/joss.01686

Yih, W., Kim, H. S., Jeong, H. J., Myung, G., and Kim, Y. G. (2004) Ingestion of cryptophyte cells by the marine photosynthetic ciliate *Mesodinium rubrum*. *Aquat. Microb. Ecol.*, **36**, 165–170. https://doi.org/10.3354/ame036165

Zhao, K.-H., Porra, R. J., and Scheer, H. (2011) Phycobiliproteins. In Roy, S., Llewellyn, C. A., Egeland, E. S., and Johnsen, G. (eds), *Phytoplankton Pigments: Characterization, Chemotaxonomy and Applications in Oceanography*. Cambridge University Press.

Zheng, G. and DiGiacomo, P. M. (2017) Remote sensing of chlorophyll-*a* in coastal waters based on the light absorption coefficient of phytoplankton. *Remote Sens. Environ.*, **201**, 331–341. https://doi.org/10.1016/j.rse.2017.09.008

Legends for Tables and Figures

Fig. 1. Light microscopy photographs of *Mesodinium rubrum* (**A**) and *Teleaulax amphioxeia* (**C**). Fluorescence microscopy photographs of *M. rubrum* (**B**) and *T. amphioxeia* (**D**) showing the fluorescence of PE 545 inside the organisms (excitation wavelength: 546 nm). **E**: Map of the French Atlantic coast, with the black square showing the spatial extent of the satellite images shown in **F** and **G**. **F, G**: False color Sentinel-2 (S2) images of a *M. rubrum* bloom, produced combining the bands 5, 3 and 2 of the S2 Multispectral Imager (MSI). The locations of 8 stations sampled on 2021/03/29 are indicated in **G**.

Fig. 2. A: Growth rate as a function of irradiance for *T. amphioxeia* (**triangles**) and *M. rubrum* (**circles**), at 17.5°C (blue) and 21°C (red). Growth curves result from an exponential Poisson model (Eq. 1) fitted on the data. K_E ± standard error is indicated for each growth curve. **B**: Cell biovolume (Equivalent Spherical Diameter, ESD) of *T. amphioxeia* and *M. rubrum* as a function of irradiance. Smaller symbols: individual replicates, bigger symbols: mean of 3 replicates, error bars: standard deviation.

Fig. 3. Concentrations of different pigments per biovolume (**A**: chl *a*, **B**: chl c_2, **C**: alloxanthin and **D**: PE 545) as a function of irradiance, in *T. amphioxeia* (triangles) and *M. rubrum* (circles), at 17.5°C (blue) and 21°C (red). Note that photoacclimation time differs between temperature conditions: 5 days for 17.5°C and 12-13 days for 21°C. Smaller symbols: individual replicates, bigger symbols: mean of 3 replicates, error bars: standard deviation.

Fig. 4. Absorption spectra of a *M. rubrum* culture (irradiance 80 µmol photons.m^{-2}.s^{-1}, mean of all replicates) measured on living cells suspended in water (grey); and using the filter-pad technique (black), with a correction for pathlength amplification.

Fig. 5. Optical properties of *T. amphioxeia* (triangles) and *M. rubrum* (circles), at 21°C, calculated using the *in vivo* absorption. **A**: Cell absorption cross section at 675 nm. **B**: chl *a*-specific absorption coefficient at 675 nm. **C**: Cell absorption cross section at 552 nm. **D**: PE 545-specific absorption coefficient at 552 nm. Smaller symbols: individual replicates, bigger symbols: mean of 3 replicates, error bars: standard deviation.

Fig. 6. Comparison of [pigment]/[chl *a*] ratios for different *M. rubrum* cultures (this study; Rial *et al.*, 2013), and pigment samples from *M. rubrum* blooms (French Atlantic coast, 2021, this study; Cariaco Basin, 2008, Guzmán *et al.*, 2016). Bar height shows the mean of all replicates, error bars show the standard deviation when available. N.A. = no data available (pigment concentration not measured).

Fig. 7. A: Chl *a* concentrations *vs in situ* $a_{phy}(665)$ derived from the above-water remote-sensing reflectance (inversion algorithm of Gons *et al.*, 2002): the blue circles represent the values for the 8 stations in the bloom. Lines represent different values of $a_{phy}^*(665)$: solid black: upper theoretical limit for $a_{phy}^*(665) = 0.0217\ m^2.mg_{chl\ a}^{-1}$ (Bricaud *et al.*, 2004); solid grey: average value of $a_{phy}^*(665) = 0.0146\ m^2.mg_{chl\ a}^{-1}$ determined by Gons *et al.* (2002) for a range of coastal ecosystems; dashed dark blue: linear regression on the correspondence of modelled $a_{phy}(665)$ and measured [chl *a*], $a_{phy}^*(665) = 0.0144\ m^2.mg_{chl\ a}^{-1}$; dashed light blue : upper ($a_{phy}^*(665) = 0.0111\ m^2.mg_{chl\ a}^{-1}$) and lower ($a_{phy}^*(665) = 0.0071\ m^2.mg_{chl\ a}^{-1}$) values of a_{phy}^* from the *M. rubrum* photoacclimation experiment (this study). **B**: [chl *a*] as a function of $a_{phy}^*(665)$, for 3 different values of $a_{phy}(665)$ (in m^{-1}). Vertical lines represent values of $a_{phy}^*(665)$ as presented in **A** (upper and lower experimental values in dashed blue; *in situ* value in dashed dark blue; Gons *et al.*, 2002 in solid grey).

Fig. 8. Maps of chl *a* concentration (in $mg.m^{-3}$) in the *M. rubrum* bloom off the coast of France, in March 2021. Sentinel-2 satellite images are the same as in Fig. 1. [Chl *a*] is derived from satellite remote-sensing reflectance using the inversion algorithm of Gons et al. (2002), with $a_{phy}^*(665) = 0{,}0144\ m^2.mg_{chl\ a}^{-1}$ **A**: 2021/03/27, **B**: 2021/03/29. Land and glint-contaminated pixels have been flagged and are colored in dark grey.

Figure 1

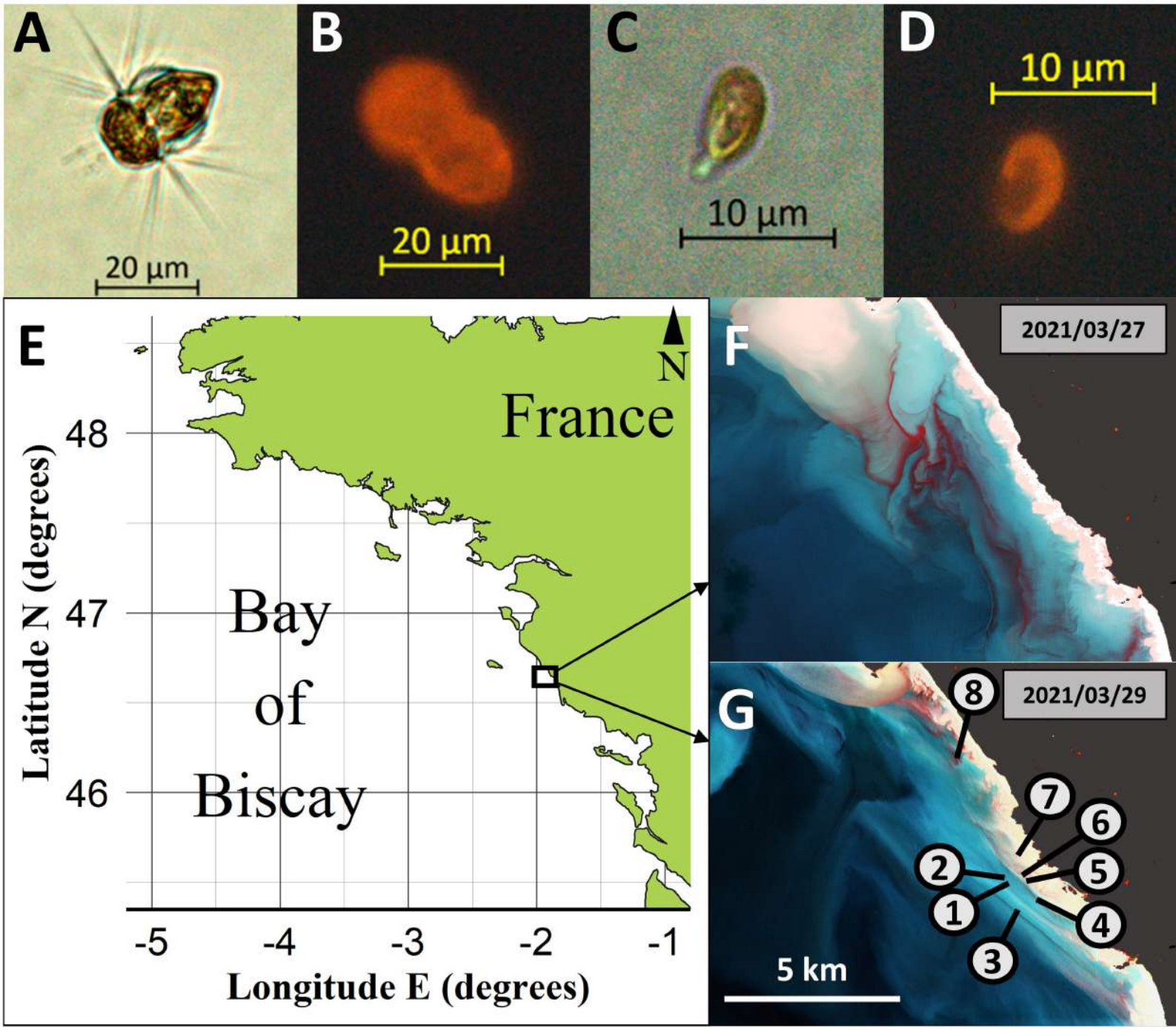
A
20 µm
B
20 µm
C
10 µm
D
10 µm
E
N
France
Bay
of
Biscay
48
47
46
-5
-4
-3
-2
-1
Latitude N (degrees)
Longitude E (degrees)
F
2021/03/27
G
2021/03/29
8
7
6
5
4
3
2
1
5 km

Figure 2

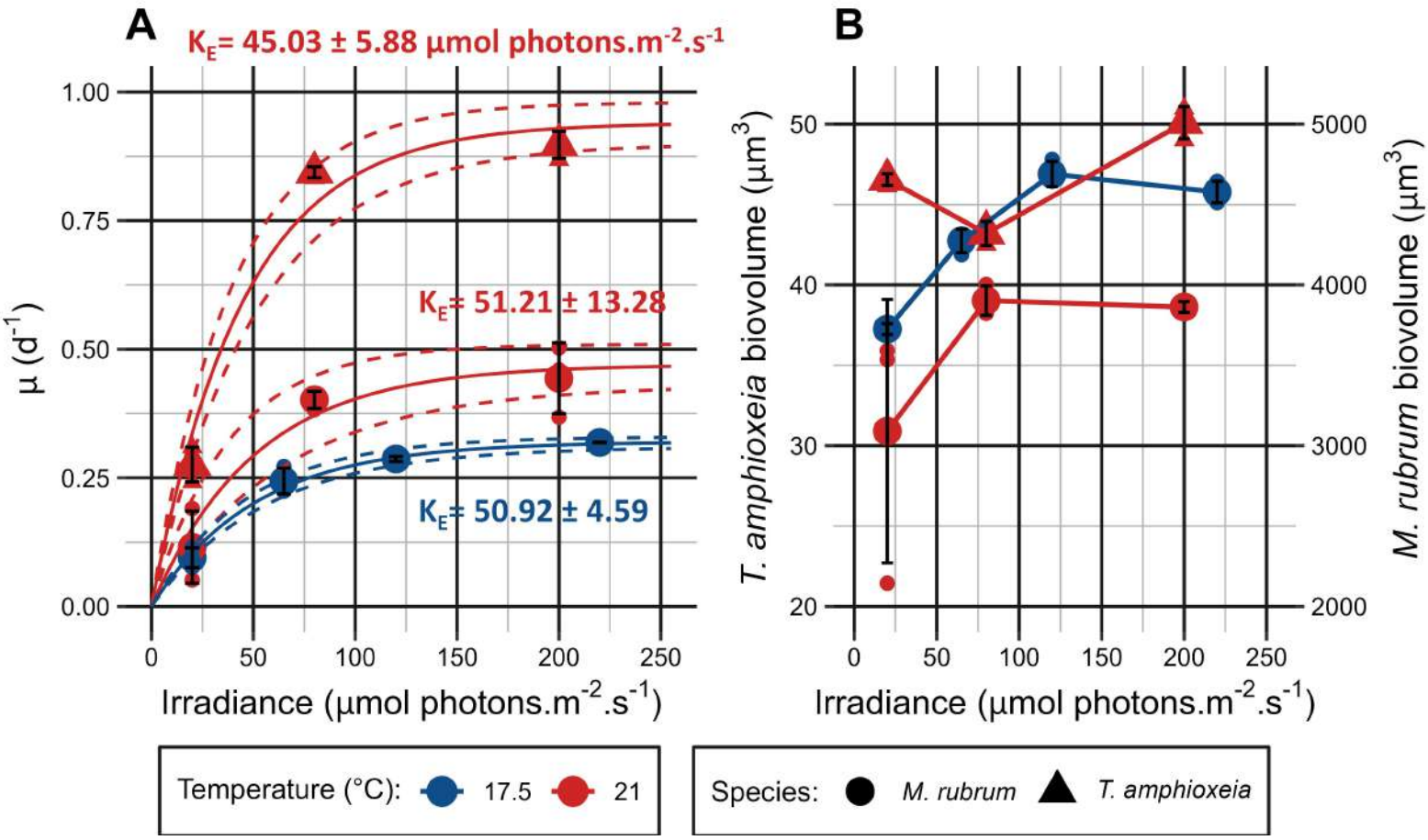
A
K_E= 45.03 ± 5.88 µmol photons.m^{-2}.s^{-1}
K_E= 51.21 ± 13.28
K_E= 50.92 ± 4.59
µ (d^{-1})
1.00
0.75
0.50
0.25
0.00
0
50
100
150
200
250
Irradiance (µmol photons.m^{-2}.s^{-1})
B
T. amphioxeia biovolume (µm^3)
M. rubrum biovolume (µm^3)
50
40
30
20
5000
4000
3000
2000
Irradiance (µmol photons.m^{-2}.s^{-1})
Temperature (°C):
17.5
21
Species:
M. rubrum
T. amphioxeia

Figure 3

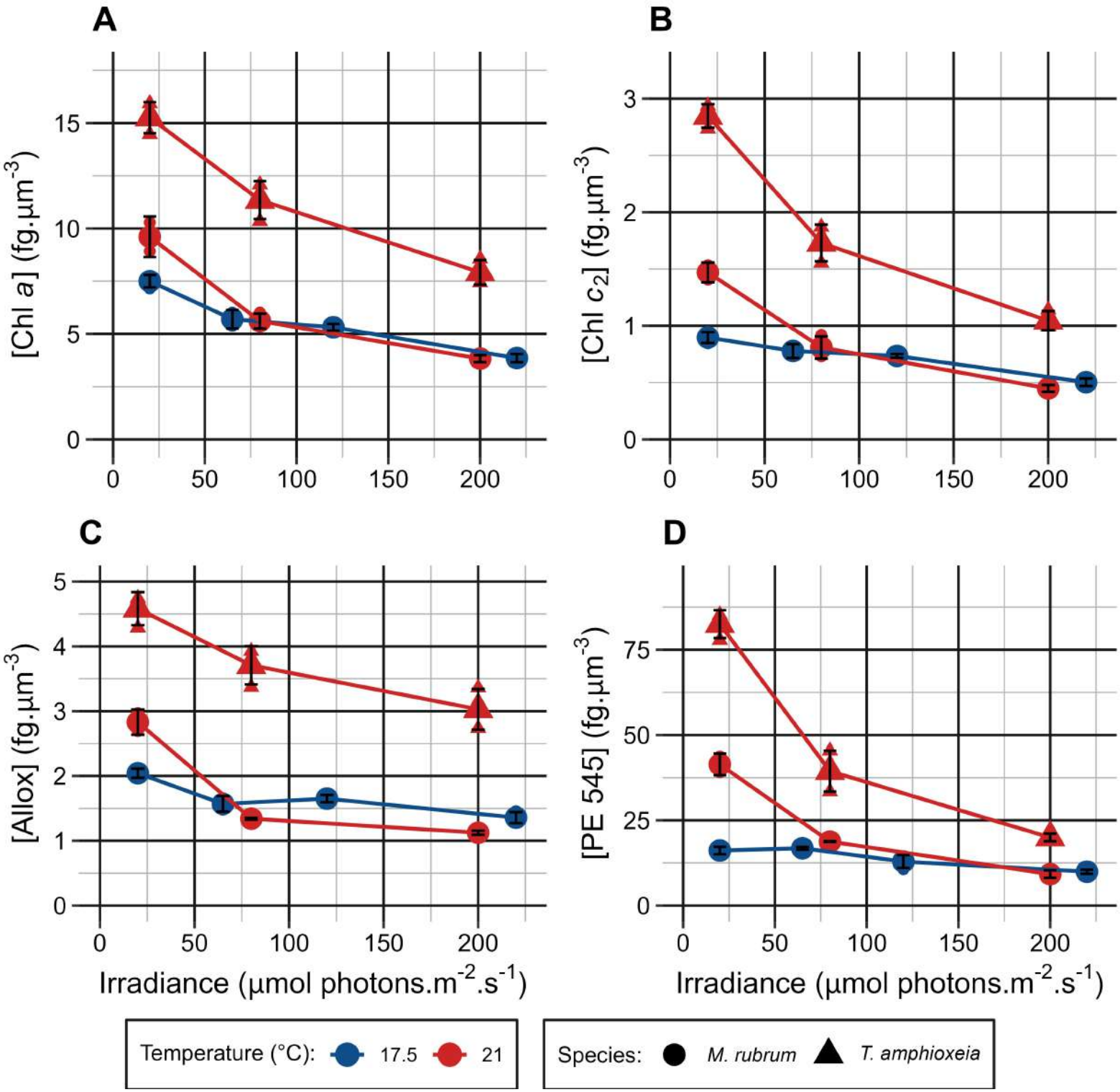
A
B
C
D
[Chl a] (fg.µm-3)
[Chl c2] (fg.µm-3)
[Allox] (fg.µm-3)
[PE 545] (fg.µm-3)
Irradiance (µmol photons.m-2.s-1)
Irradiance (µmol photons.m-2.s-1)
Temperature (°C): 17.5 21
Species: M. rubrum T. amphioxeia

Figure 4

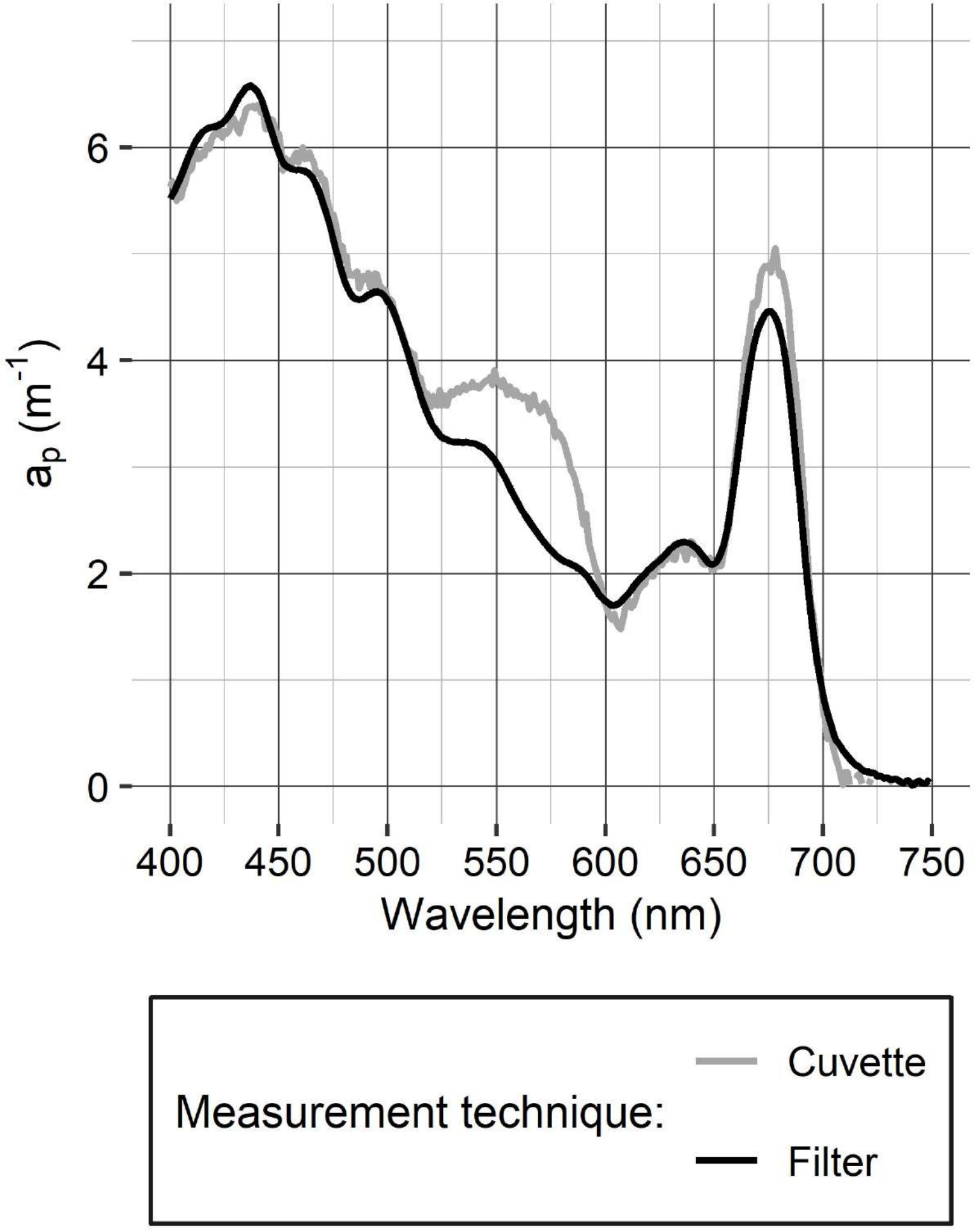
6
4
2
0
a_p (m^{-1})
400
450
500
550
600
650
700
750
Wavelength (nm)
Measurement technique:
Cuvette
Filter

Figure 5

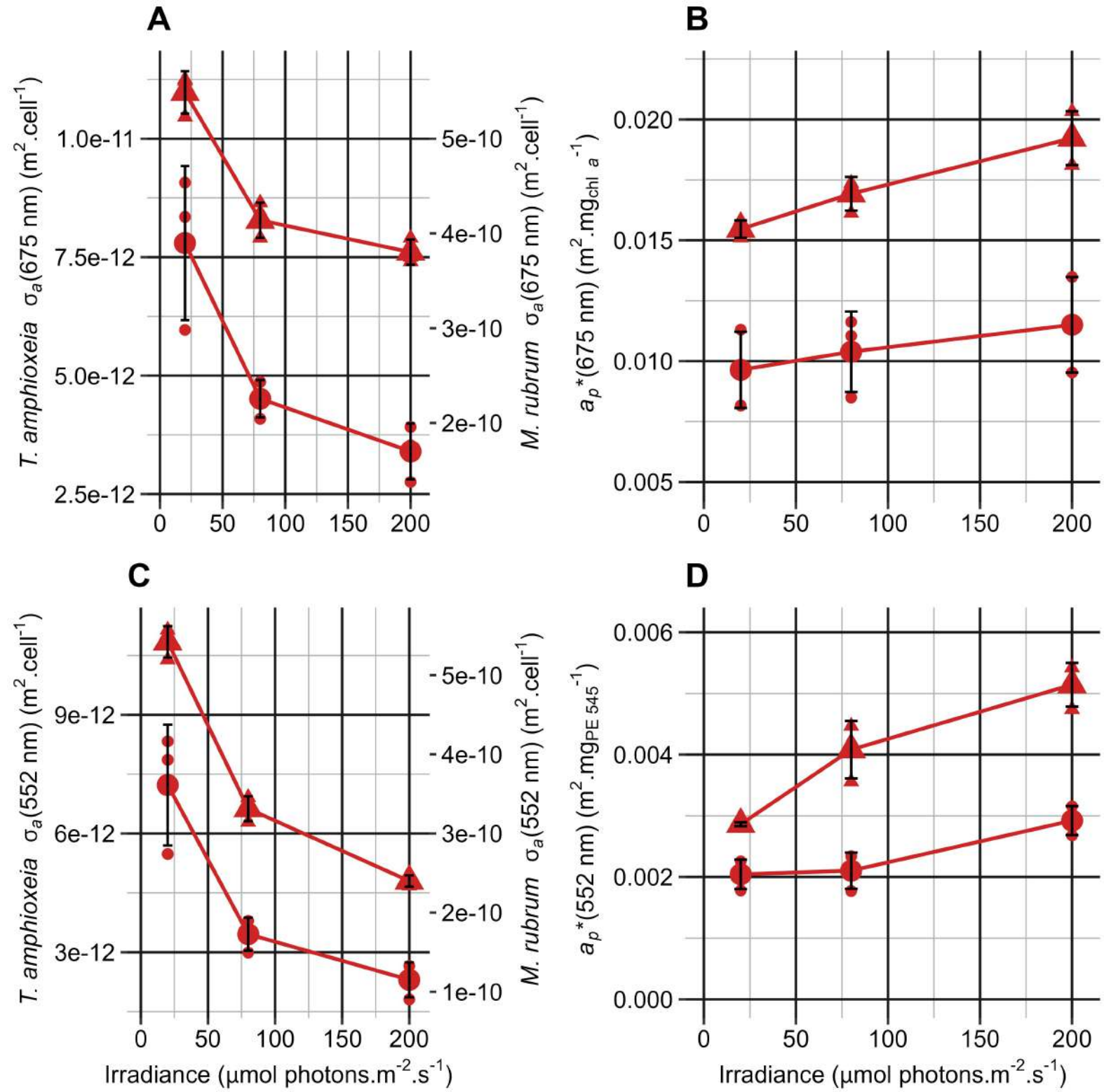
A
B
C
D
T. amphioxeia σa(675 nm) (m2.cell-1)
M. rubrum σa(675 nm) (m2.cell-1)
ap*(675 nm) (m2.mgchl a-1)
T. amphioxeia σa(552 nm) (m2.cell-1)
M. rubrum σa(552 nm) (m2.cell-1)
ap*(552 nm) (m2.mgPE 545-1)
Irradiance (µmol photons.m-2.s-1)
1.0e-11
7.5e-12
5.0e-12
2.5e-12
5e-10
4e-10
3e-10
2e-10
0.020
0.015
0.010
0.005
9e-12
6e-12
3e-12
1e-10
0.006
0.004
0.002
0.000
0
50
100
150
200

Figure 6

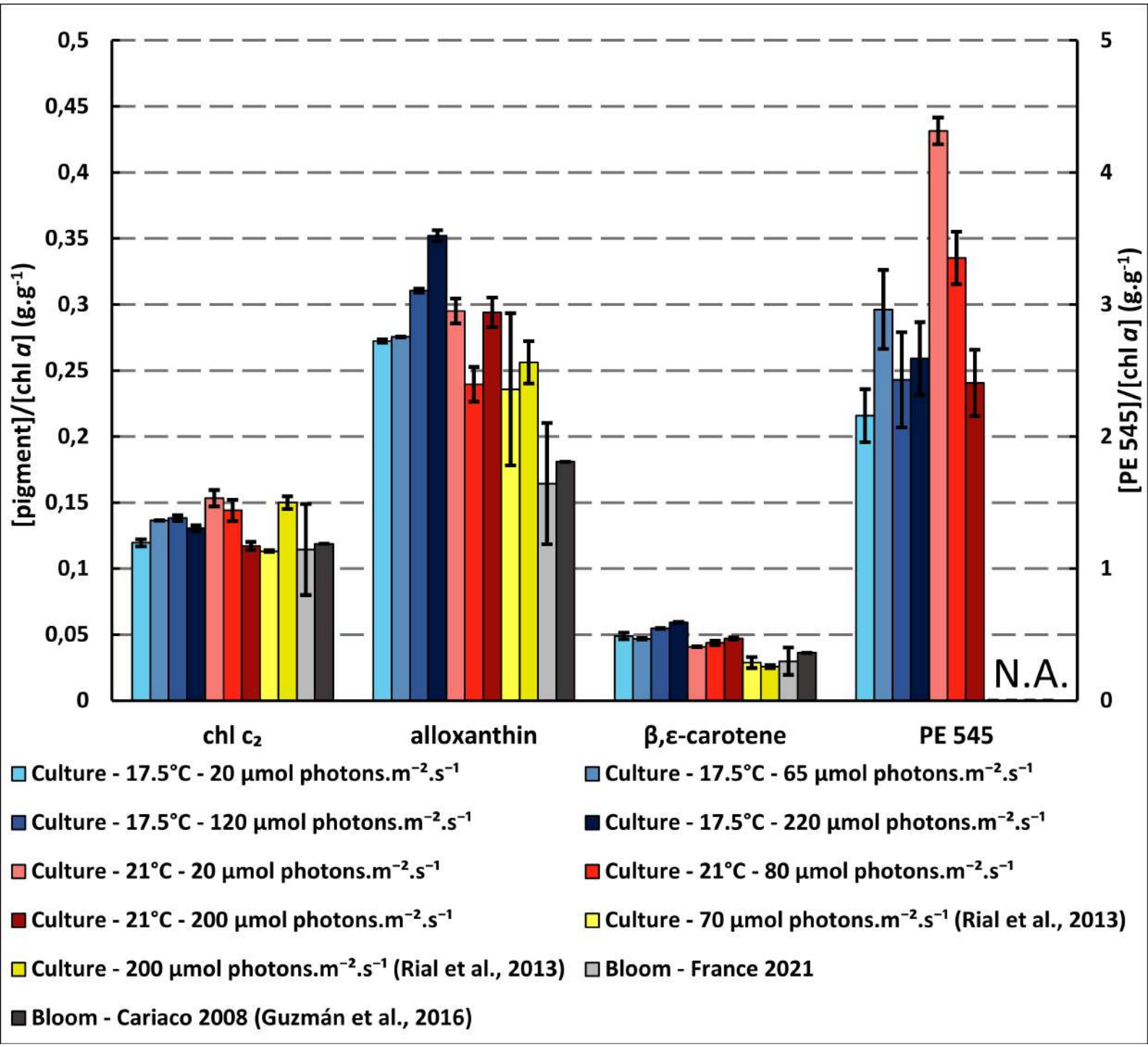
0,5
0,45
0,4
0,35
0,3
0,25
0,2
0,15
0,1
0,05
0
5
4
3
2
1
0
[pigment]/[chl a] (g.g-1)
[PE 545]/[chl a] (g.g-1)
N.A.
chl c2
alloxanthin
β,ε-carotene
PE 545
Culture - 17.5°C - 20 µmol photons.m-2.s-1
Culture - 17.5°C - 65 µmol photons.m-2.s-1
Culture - 17.5°C - 120 µmol photons.m-2.s-1
Culture - 17.5°C - 220 µmol photons.m-2.s-1
Culture - 21°C - 20 µmol photons.m-2.s-1
Culture - 21°C - 80 µmol photons.m-2.s-1
Culture - 21°C - 200 µmol photons.m-2.s-1
Culture - 70 µmol photons.m-2.s-1 (Rial et al., 2013)
Culture - 200 µmol photons.m-2.s-1 (Rial et al., 2013)
Bloom - France 2021
Bloom - Cariaco 2008 (Guzmán et al., 2016)

Figure 7

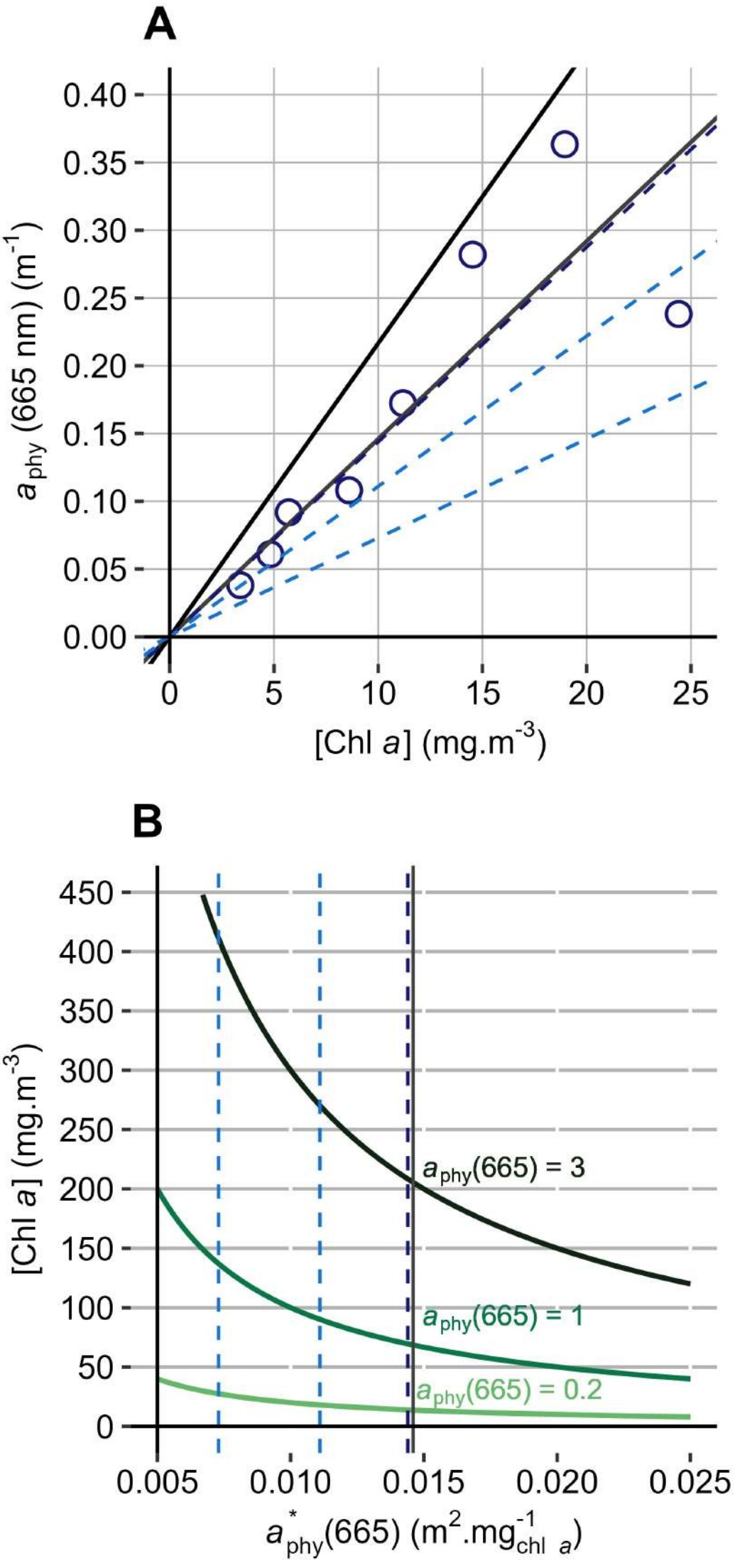
A
0.40
0.35
0.30
0.25
0.20
0.15
0.10
0.05
0.00
a_{phy} (665 nm) (m^{-1})
0
5
10
15
20
25
[Chl *a*] ($mg.m^{-3}$)
B
450
400
350
300
250
200
150
100
50
0
[Chl *a*] ($mg.m^{-3}$)
$a_{phy}(665) = 3$
$a_{phy}(665) = 1$
$a_{phy}(665) = 0.2$
0.005
0.010
0.015
0.020
0.025
$a^{*}_{phy}(665)$ ($m^2.mg^{-1}_{chl\ a}$)

Figure 8

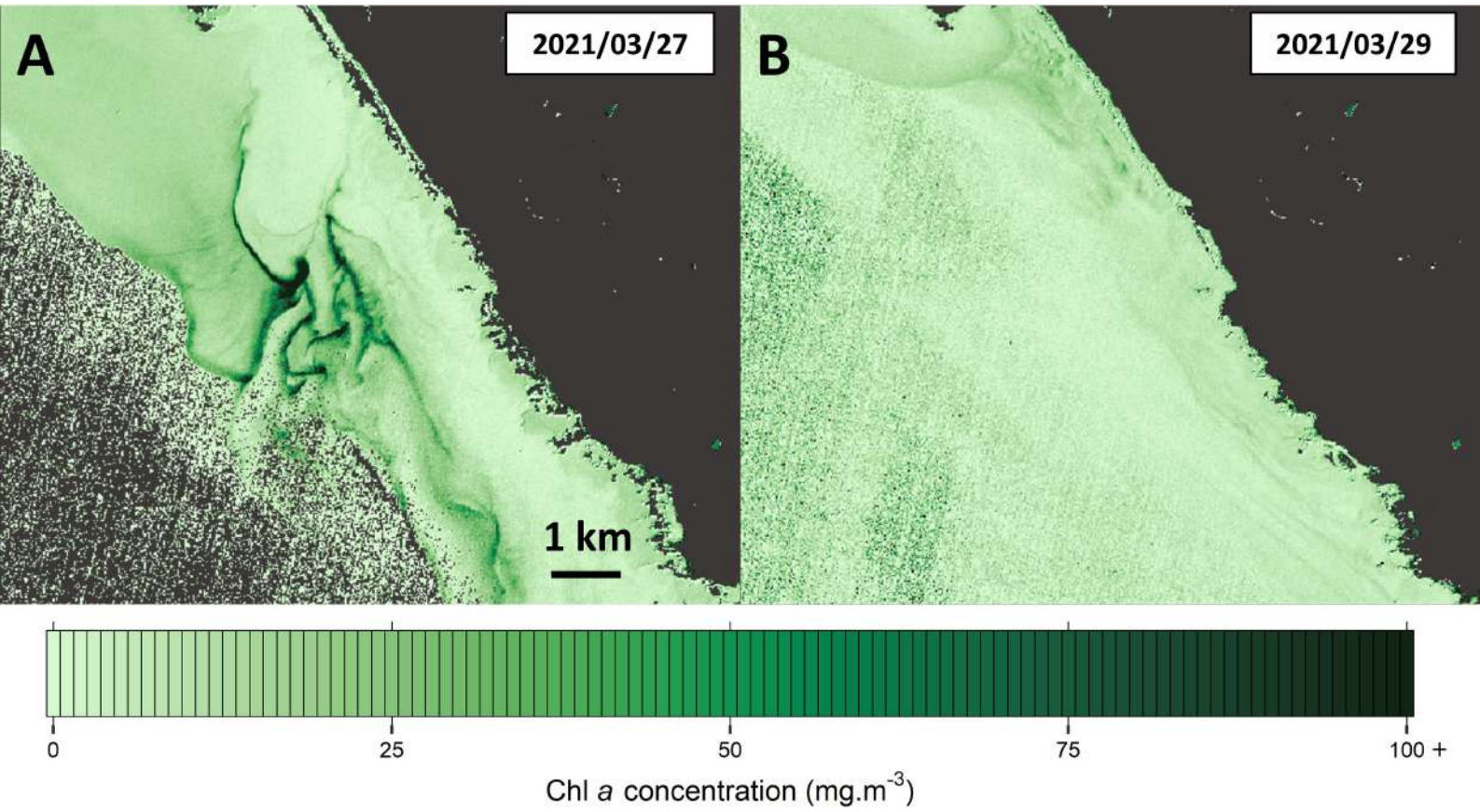
A
2021/03/27
1 km
B
2021/03/29
0
25
50
75
100 +
Chl a concentration (mg.m-3)

Supplementary material for the article "Photoacclimation in the kleptoplastidic ciliate *Mesodinium rubrum* and its cryptophyte prey *Teleaulax amphioxeia*: phenotypic variability and implications for red tide remote sensing"

Authors:

Victor Pochic[1,2,*], Pierre Gernez[1], Maria Laura Zoffoli[3], Véronique Séchet[2], Liliane Carpentier[2], Thomas Lacour[2]

[1] Nantes Université, Institut des Substances et Organismes de la Mer, ISOMER, UR 2160, F-44000 Nantes, France

[2] Ifremer, PHYTOX, Laboratoire PHYSALG, F-44000 Nantes, France

[3] Consiglio Nazionale delle Ricerche, Istituto di Scienze Marine (CNR-ISMAR), 00133, Rome, Italy

[*]Corresponding author. Contact: victor.pochic@univ-nantes.fr

Supplementary Information 1: Pathlength amplification corrections for absorption measured using the filter-pad technique.

Non-specific pathlength amplification correction as in Stramski *et al.* (2015):

Particulate absorption coefficients measured with the filter-pad technique were corrected for pathlength amplification by a power law proposed by Stramski *et al.* (2015), as in the following equation:

$$a_{\mathrm{p}}^{\mathrm{standard}}(\lambda) = 0.323\, a_{\mathrm{p}}^{\mathrm{uncorr}}(\lambda)^{1.0867} \qquad \textit{Supp. Equation 1.}$$

Where $a_{\mathrm{p}}^{\mathrm{standard}}(\lambda)$ is the corrected absorption at wavelength λ (in m^{-1}); $a_{\mathrm{p}}^{\mathrm{uncorr}}(\lambda)$ the raw absorption measured with the filter-pad technique.

Specific pathlength amplification correction taking the in vivo absorption as reference:

The specific pathlength amplification correction was applied by fitting the filter-pad absorption measurements, for each sample, to the corresponding *in vivo* absorption measurements that were taken as reference as proposed in Röttgers and Gehnke (2012).

The wavelength range was 400-500 and 600-700 nm. Wavelengths below 400 nm or above 700 nm were excluded because of uncertainty in the measurements with the spectrophotometer. Additionally, wavelengths between 500 and 600 nm were excluded because the filter-pad technique leads to a distortion of the spectral shape in the area where PE 545 absorbs (see Fig. 4), preventing the match with the *in vivo* absorption.

The correction was taken as the best fit of a power law with 2 parameters a and b, such as:

$$a_p(\lambda) = \mathrm{a}.\, a_{\mathrm{p}}^{\mathrm{uncorr}}(\lambda)^b \qquad \textit{Supp. Equation 2.}$$

Where $a_{\mathrm{p}}(\lambda)$ is the *in vivo* absorption at wavelength λ (in m^{-1}); $a_{\mathrm{p}}^{\mathrm{uncorr}}(\lambda)$ the raw absorption measured with the filter-pad technique.

Therefore, we obtained a specific pathlength amplification correction for each sample. A mean correction (± standard deviation) was calculated by taking the mean of parameters a and b (± standard deviation) for all corrections. This correction is shown in Fig. S5 and compared to the non-specific pathlength amplification correction of Stramski et al. (2015).

Supplementary Information 2: Calculation of the proportion of *M. rubrum* PE 545 originating from predation vs *de novo* synthesis.

PE 545 total production by *Mesodinium* (including *de novo* synthesis and predation) can be computed as follows:

$P_{PE\ 545} = \mu\ .\ Q_{Meso} = 0.44$ x 39.20 = 17.38 pg $Cell^{-1}$ d^{-1}

With Q_{Meso} is the PE 545 per *Mesodinium* cell (pg $cell^{-1}$) acclimated to 200µE and µ the growth rate of *Mesodinium* (d^{-1}).

We can also compute the amount of PE 545 acquired from ingested preys:

$I_{PE\ 545} = G\ .\ Q_{Tel} = 1$ x 3.79 = 3.79 pg $cell^{-1}$ d^{-1}

With Q_{Tel} is the PE 545 per *Teleaulax* cell (pg $cell^{-1}$) acclimated to 20µE and G the ingestion rate of *Mesodinium* (*Teleaulax* cell.*Mesodinium* $cell^{-1}.d^{-1}$). To estimate the maximum contribution of ingestion we consider that all the available prey were ingested (1 prey per Cell per day, as *M. rubrum* cultures were fed every 3 days at a prey/predator ratio of 3/1) and all the PE 545 is transferred to *Mesodinium*.

$$\frac{I_{PE\ 545}}{P_{PE\ 545}} = \frac{3.79}{17.38} = 0.22$$

It shows that PE 545 from *Teleaulax* can contribute up to 22% of overall *Mesodinium* PE 545. Considering all the other prey pigments that are likely to present similar (albeit lower) contributions, this is a non-negligible contribution to the overall pigment content of the predator cell.

Supplementary Table

Supplementary Table SI

Table. SI. Variability in [chl *a*] derived from the algorithm of Gons et al. (2002), depending on a_{phy}*(665) and a_{phy}(665).

[chl *a*] (mg.m^{-3})				percentage of variation compared to a_{phy}*(665) = 0,0146 m^2.mg$_{chl\ a}^{-1}$			absolute variation of [chl *a*] (in mg.m^{-3}) compared to a_{phy}*(665) = 0,0146 m^2.mg$_{chl\ a}^{-1}$			
a_{phy}*(665) (m^2.mg$_{chla}^{-1}$)	a_{phy}(665) = 0.2 m^{-1}	a_{phy}(665) = 1 m^{-1}	a_{phy}(665) = 3 m^{-1}	a_{phy}(665) = 0.2 m^{-1}	a_{phy}(665) = 1 m^{-1}	a_{phy}(665) = 3 m^{-1}	a_{phy}(665) = 0.2 m^{-1}	a_{phy}(665) = 1 m^{-1}	a_{phy}(665) = 3 m^{-1}
0.0071	28.2	140.8	422.5	105.6	105.6	105.6	14.5	72.4	217.1
0.0111	18.0	90.1	270.3	31.5	31.5	31.5	4.3	21.6	64.8
0.0144	13.9	69.4	208.3	1.4	1.4	1.4	0.2	1.0	2.9
0.0146	13.7	68.5	205.5	0.0	0.0	0.0	0.0	0.0	0.0
0.0217	9.2	46.1	138.2	-32.7	-32.7	-32.7	-4.5	-22.4	-67.2

Supplementary figures

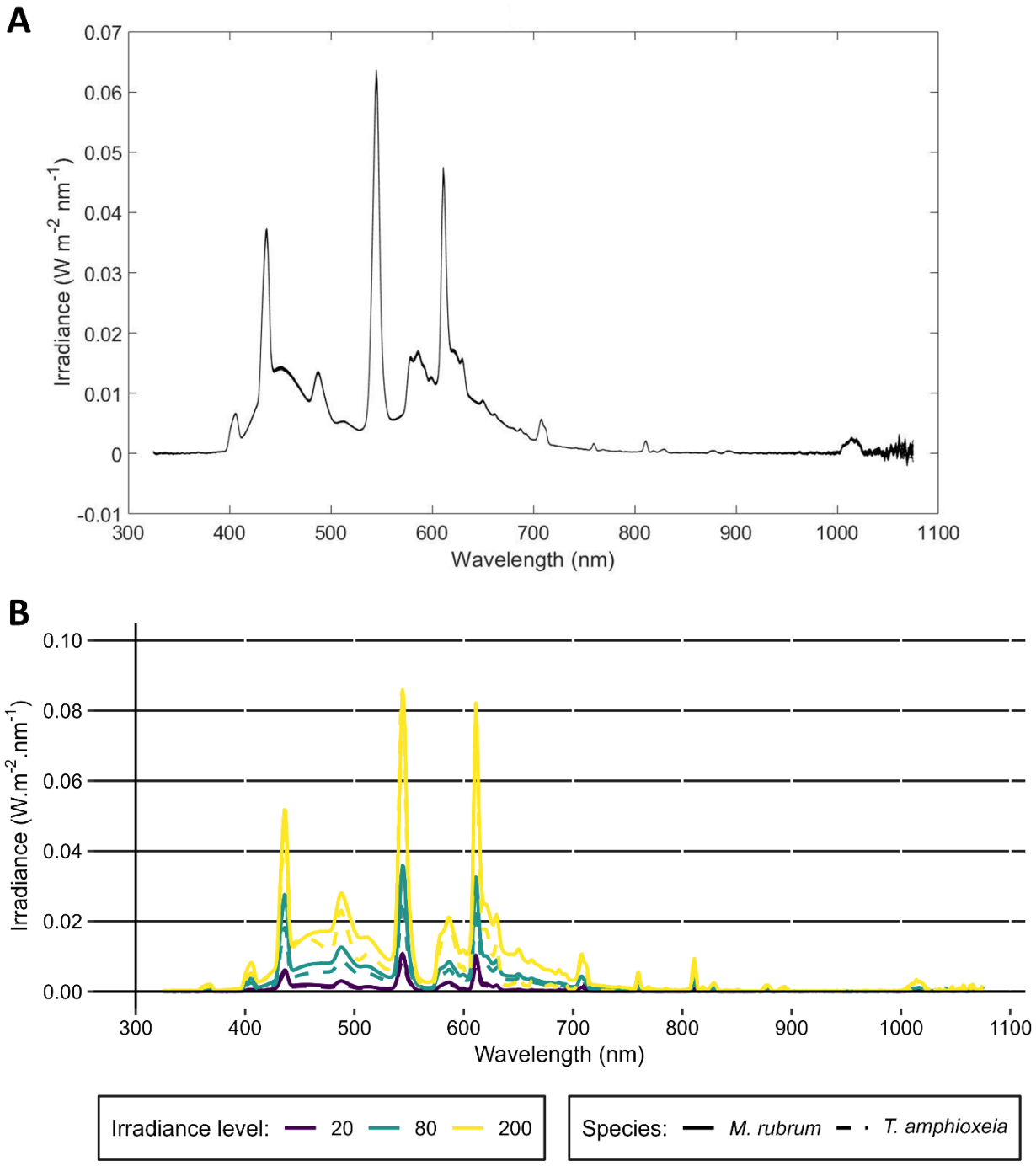

Fig. S1. Irradiance spectra of the culture light measured with a portable spectroradiometer (ASD Fieldspec, Handheld 2) **A**: First photoacclimation experiment (differences between irradiance levels were not assessed). **B**: Second photoacclimation experiment.

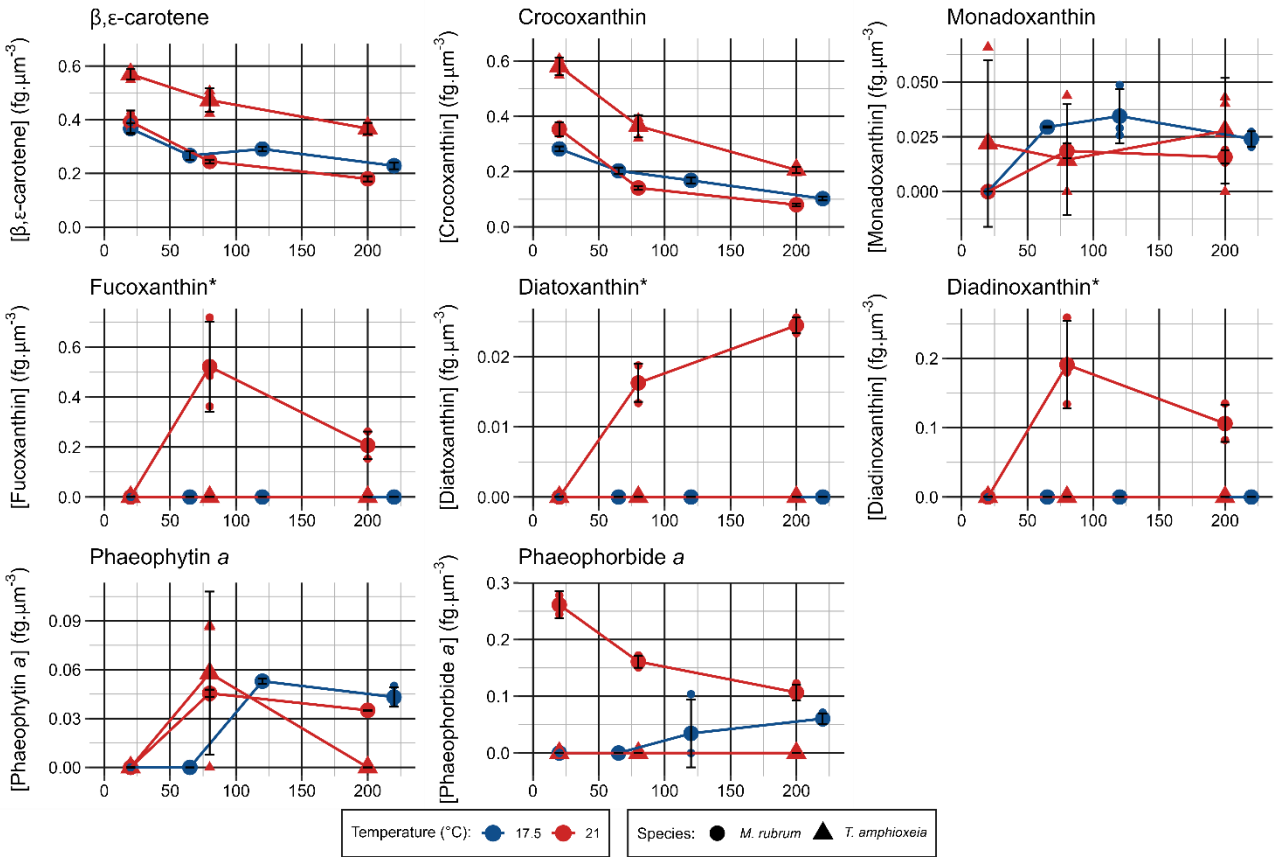

Fig. S2. Concentration of minor pigments (in fg.µm^{-3}) in the cultures. Asterisks mark the pigments absent in cryptophytes, that come from the contamination by small brown microalgae.

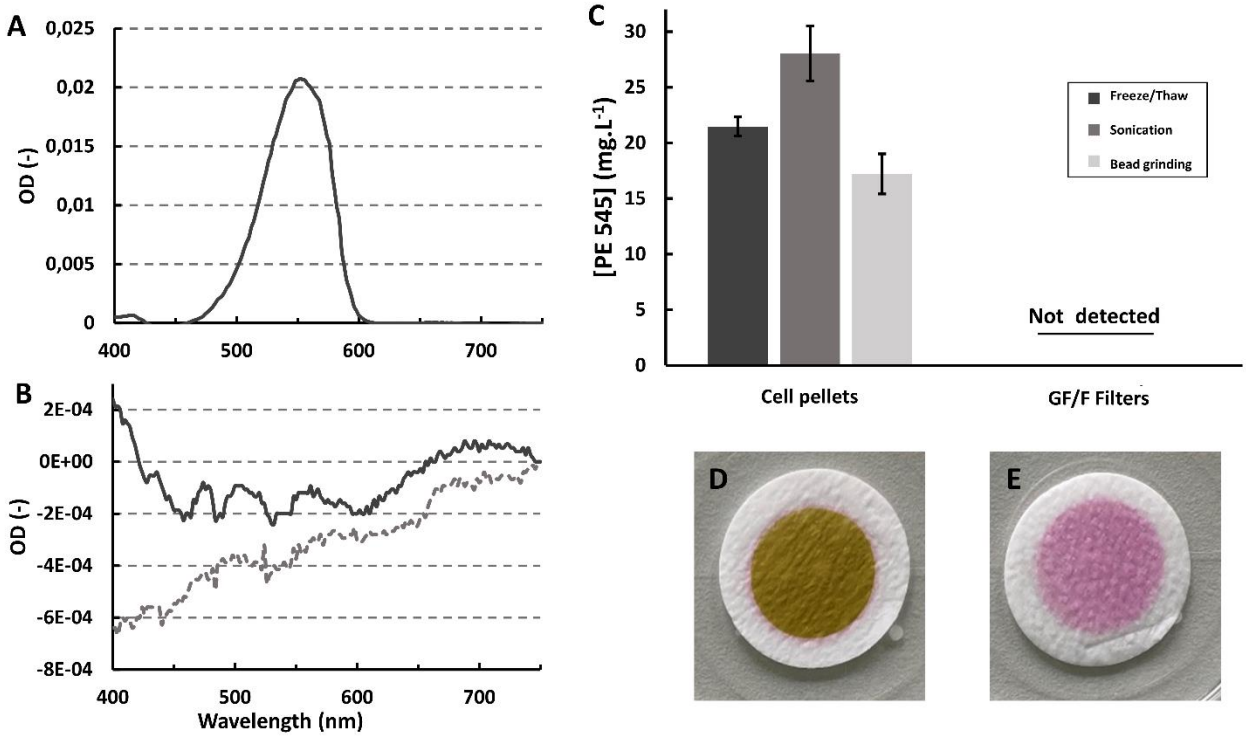

Fig. S3. A: Absorption spectrum of the extract from a centrifugated cell pellet, sonicated. **B:** Absorption spectra from filtered samples, extracted in phosphate buffer (dashed line) and in phosphate buffer + glycerol (solid line). **C:** Comparison of extraction efficiency between cell pellets and GF/F filters, with 3 methods of extraction in phosphate buffer. **D, E**: GF/F filters with *T. amphioxeia* after freezing at -80°C, front (**D**) and back (**E**)

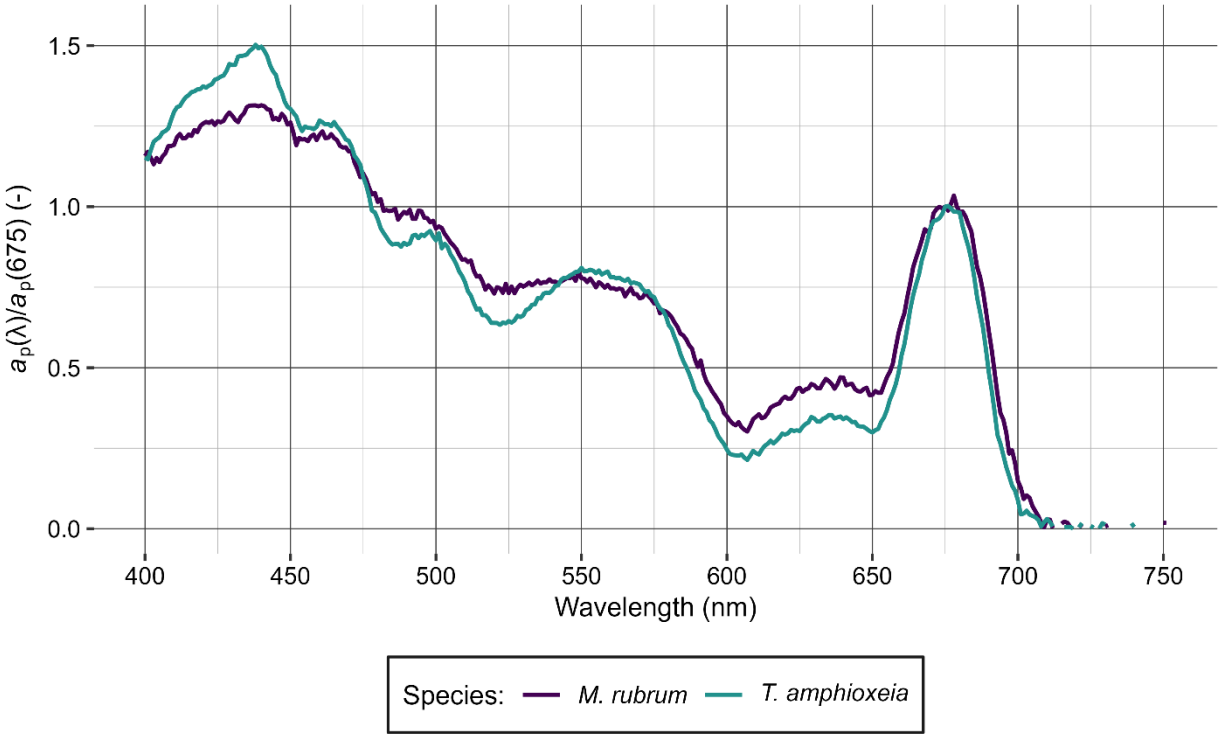

Fig. S4. Absorption spectra of *T. amphioxeia* and *M. rubrum* (cultures at 80 µmol photons.m^{-2}.s^{-1}, mean of 3 replicates), standardized by the value of $a_p(675)$.

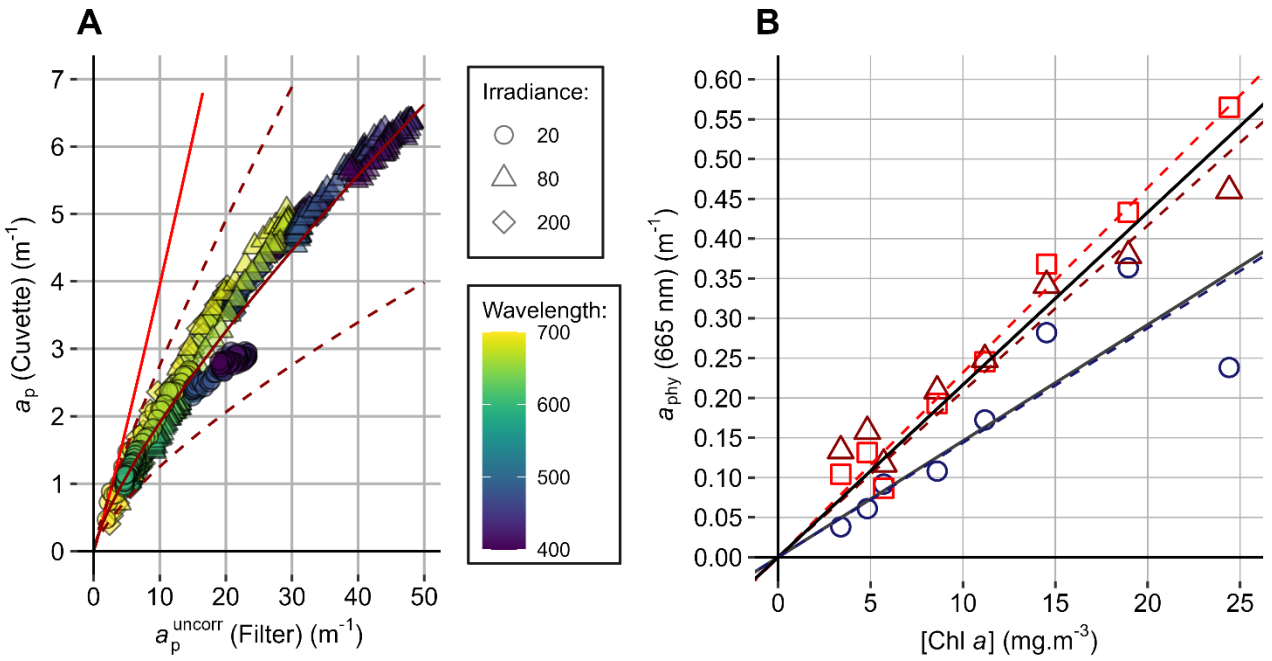

Fig. S5. A: Scatter plot of a_p measured *in vivo* on a suspension of cells vs a_{phy} measured on GF/F filters with the filter pad technique. Values of a_p are the mean of 3 replicates for each irradiance. The solid light red curve represents the non-specific pathlength amplification correction proposed by Stramski et al. (2015). The dark red curves represent the specific pathlength correction fitted on the data, mean (solid) ± standard error (dashed). **B:** Chl *a* concentrations *vs in situ* $a_{phy}(665)$ at the 8 stations in the bloom. Dark blue circles: modelled $a_{phy}(665)$ obtained with the inversion algorithm of Gons et al. (2002). Light red squares: filter-pad measured aphy(665) with non-specific pathlength amplification correction of Stramski et al., 2015. Dark red triangles: filter-pad measured $a_{phy}(665)$ with specific pathlength amplification correction derived from experiments in this study. Lines represent different values of $a_{phy}^*(665)$: solid black: upper theoretical limit for $a_{phy}^*(665)$ (Bricaud *et al.*, 2004); solid grey: average value of a_{phy}^* determined by Gons *et al.* (2002) for a range of coastal ecosystems; dashed lines represent the best linear fit for each of the 3 sets of values for $a_{phy}(665)$.

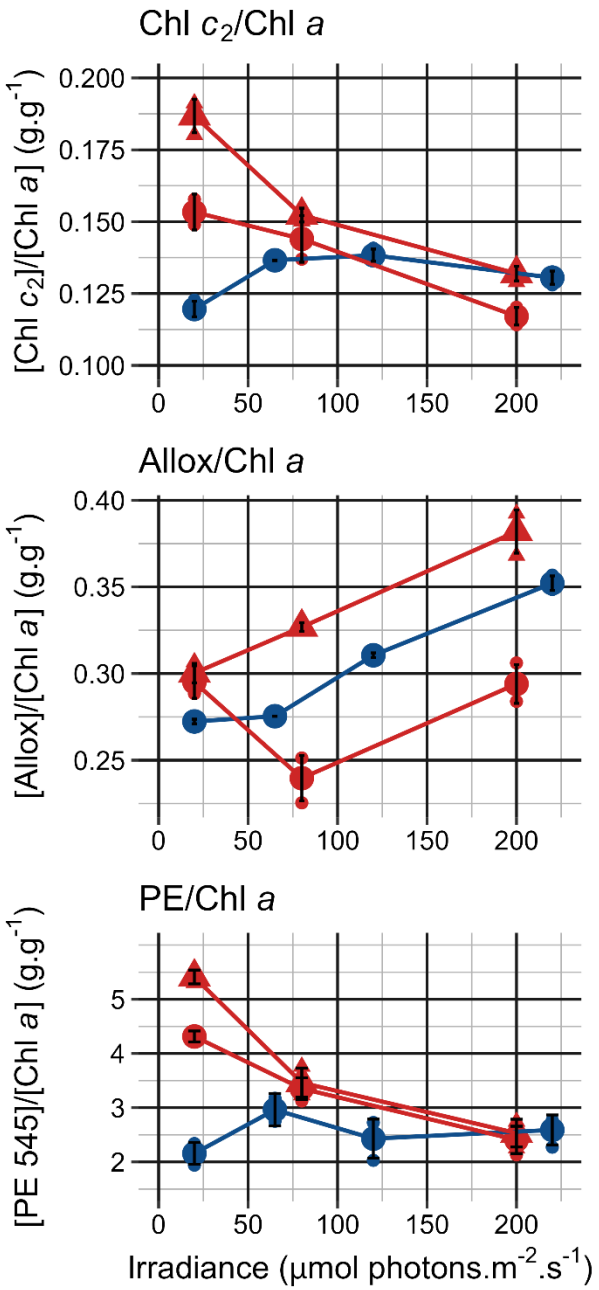

Fig. S6. [Pigment]/[chl a] ratios (in g.g$_{chl\ a}^{-1}$) in the cultures of the photoacclimation experiments, in *T. amphioxeia* (triangles) and *M. rubrum* (circles), at 17.5°C (blue) and 21°C (red).